Fachbereich Mathematik und Naturwissenschaften
Fachgruppe Physik
Bergische Universität Wuppertal

Cross-section measurement of t-channel single top-quark production at $\sqrt{s} = 13$ TeV with the ATLAS detector at the LHC

Master Thesis
von
Gunnar Jäkel

1. September 2015

Contents

1 Introduction **1**

2 Top-Quark production at the LHC **3**
2.1 The Standard Model 3
2.2 Top-quarks 4
2.3 Single top-quark 6
2.4 Background processes 7

3 LHC and the ATLAS Detector **11**
3.1 Large Hadron Collider 11
3.2 The ATLAS Detector 13
3.3 The coordinate system 14
3.4 Dataset of this analysis 15

4 Monte Carlo generators **19**
4.1 Particle collisions 19
4.2 Monte-Carlo generators 21
4.3 Monte-Carlo samples 22

5 Object reconstruction and event selection **25**
5.1 Tracking 25
5.2 Vertex reconstruction 25
5.3 Charged lepton reconstruction 26
5.4 Jet reconstruction 26
5.5 Missing transverse momentum 27

6 Background modeling **29**
6.1 Multijet background estimation 29
6.2 W+jets control region 32

7 Signal extraction **37**
7.1 Neural networks 37
7.2 Input variables 38
7.3 Training results 42

8 Cross-section measurement **47**
8.1 Fit to the *NNout* discriminant 47
8.2 Inclusive cross-section measurement 51

9 Conclusion **53**

List of Figures **55**

List of Tables **58**

Bibliography **59**

1 Introduction

Physics is the science, that describes nature on all scales. The theory of general relativity, for example, describes gravitation, the evolution of galaxies and the whole visible universe. But physics is also about small scales, like condensed matter physics, that describes solid matter consisting of atom-lattices. On even smaller scales there are molecules and atoms, which are also parts of chemistry. An atom is dividable in electrons, which are elementary particles, and an atomic nucleus, that consists of protons and neutrons. Protons and neutrons are hadrons and consist of quarks and gluons, which hold the hadrons together. To current knowledge these quarks and gluons are elementary particles, just like the electron. To understand physics as a whole and hence nature, a detailed knowledge of the smallest particles is necessary. The heaviest known elementary particle is the top quark. It has a mass of $m = 173.3 \pm 0.27 \pm 0.71$ GeV [1] and is therefore ≈ 40 times heavier than the second heaviest quark, the bottom quark. Because of the high mass, the top-quark has a very short lifetime of $\tau = 5 \cdot 10^{-25}$ s. The timescale for hadronisation is $t = 10^{-23}$ s, therefore the top quark is the only quark, that doesn't hadronise before it decays. This is the reason, why the mass of the top quark is directly accessible through kinematic reconstruction methods. The high mass of the top quark is also important in theoretical predictions of cross sections. This is, because in loop-corrections the mass of the circulating particle enters, and therefore the top-quark correction is the dominant contribution. Another important property, besides the mass, is the cross section. It describes the probability to produce the top quark in a certain process. The most probable channel to produce a top quark is the $t\bar{t}$-channel, where a top quark and a top antiquark are produced together. But to understand the complete Standard Model (SM) all production modes have to be measured. For example searches are ongoing to discover the tH- and the tZ-channel, where one top-quark is produced in association with a Higgs- or a Z-Boson. To discover rarely appearing processes a precise knowledge of the more probable processes is necessary. One of these processes is the single top-quark production, where just one top-quark or top-antiquark is produced. The channel with the highest cross section in single top-quark production is the t-channel. For 7 TeV and 8 TeV the total and differential cross sections were measured with the ATLAS (A Toroidal LHC ApparatuS) detector [2]-[6]. The next step is to repeat this measurement for 13 TeV. The aim of this thesis is to establish the signal in pp collisions at 13 TeV and to give a first measurement with the early Run2 data of the LHC. This cross section was calcu-

lated in NNLO accuracy [7] to be $\sigma_t = 136.02^{+5.40}_{-4.57}$ pb^{-1} for top-quark production and $\sigma_{\bar{t}} = 80.95^{+4.06}_{-3.61}$ pb^{-1} for top-antiquark production.

In chapter 2 a brief introduction to the SM and top-quark physics is provided. Chapter 3 contains information about the LHC, the ATLAS detector and the analyzed data set. Event generation with Monte Carlo generators is explained in chapter 4. Different reconstruction methods of particles used in this analysis are provided in chapter 5. In chapter 6 the modeling of the background processes is studied. To separate signal and background processes a neural network is introduced in chapter 7. The cross section of t-channel single top-quark production is calculated in chapter 8.

$\sigma_t = 136.0^{+5.4}_{-4.6}$ pb^{-1} for top-quark production and $\sigma_{\bar{t}} = 81.0^{+4.1}_{-3.6}$ pb^{-1}

2 Top-Quark production at the LHC

The top-quark is to today's knowledge an elementary particle. It doesn't exist in nature as a free particle, because of its short lifetime, but has to be produced in particle colliders. This chapter contains a brief introduction of particle physics. Afterwords a more detailed description of the production and decay of top-quarks and especially single top-quarks is presented. At the end background processes of the single top-quark analysis are mentioned.

2.1 The Standard Model

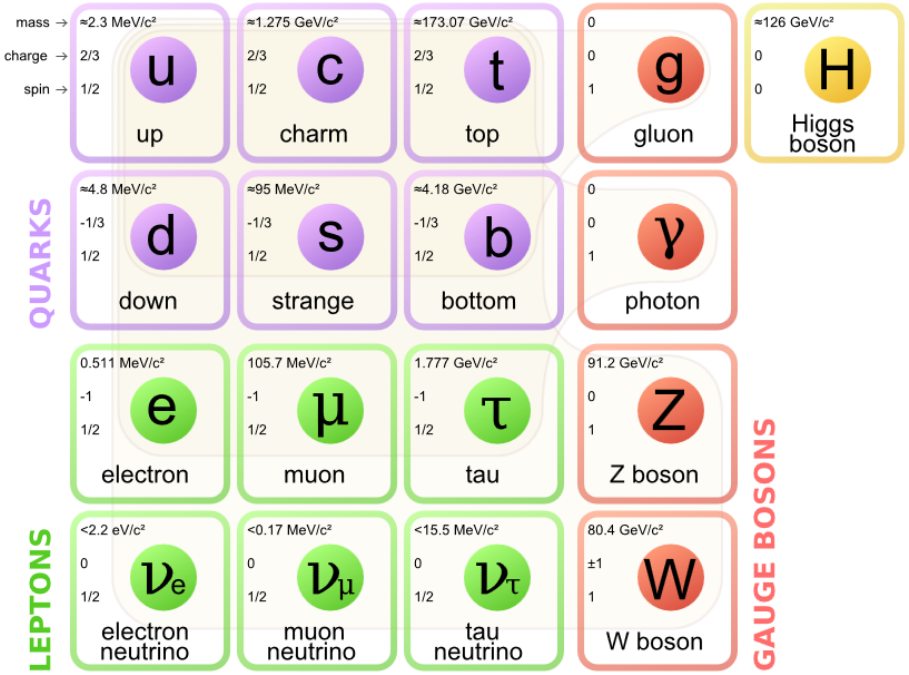

Figure 2.1: *Elementary particles of the standard model. The graphic is taken from Ref. [8].*

In modern physics there are four known forces. These forces are the strong force, the weak force, the electromagnetic force and gravitation. Gravitation is described by the theory of general relativity and explains the large structures of the universe. The other three forces are described by the Standard Model of particle physics (SM). Detailed information about the SM can be found elsewhere, i.g. in Ref. [9]. Within the SM the weak and the electromagnetic force are united to the electroweak force. The SM is a quantum field theory, which describes the fundamental particles and the interactions between them. According to their spin the particles can be divided into fermions, which are the particles matter is made of and have half-integer spin. In contrast, the bosons, which are the particles mediating a force, have integer spin. All of the particles in the SM are shown in Figure 2.1. Additionally, each particle has a corresponding antiparticle, which has the same properties as the particle, just with the opposite charge.

Each force is associated with a boson, that mediates this force. The photon is the mediator of the electromagnetic force and interacts with all electrically charged particles. The gluon is the mediator of the strong force and interacts with all particles that carry a color charge. These particles are the quarks and the gluon itself. Because of color confinement, colored particles can not be isolated, but form hadrons. The W- and Z-bosons are the mediators of the weak force. All fermions and the W- and Z-bosons themself interact via the weak force.

For the three down-type quarks there are two different representations. The mass eigenstates d, s, b and the weak-interaction eigenstates d', s', b'. They are connected with each other by the CKM (Cabibbo-Kobayashi-Maskawa) matrix [10],[11], such that

$$\begin{pmatrix} d' \\ s' \\ b' \end{pmatrix} = \begin{pmatrix} V_{ud} & V_{us} & V_{ub} \\ V_{cd} & V_{cs} & V_{cb} \\ V_{td} & V_{ts} & V_{tb} \end{pmatrix} \begin{pmatrix} d \\ s \\ b \end{pmatrix} \tag{2.1}$$

The coupling of a down-type quark with an up-type quark is then determined by the CKM matrix. The CKM matrix is almost the unity matrix, therefore the coupling in one generation of quarks is much larger than the coupling to another generation.

2.2 Top-quarks

The heaviest elementary particle in the SM is the top-quark with a mass of $m_t \approx 173.5$ GeV. It has a spin of $\frac{1}{2}$ and an electric charge of $+\frac{2}{3}e$, where e is the elementary charge. The lifetime of the top-quark is $\tau_t \approx 5 \cdot 10^{-25}$ s, therefor it is the only quark that cannot form a bound state via the strong force, which would take around

10^{-23} s. Because of the high mass, the top quark can only be produced in high energy collisions and decays almost instantly due to the short life time. Therefore the only possibility to study the properties of the top-quark is to build a particle accelerator, like the Large Hadron Collider (LHC).

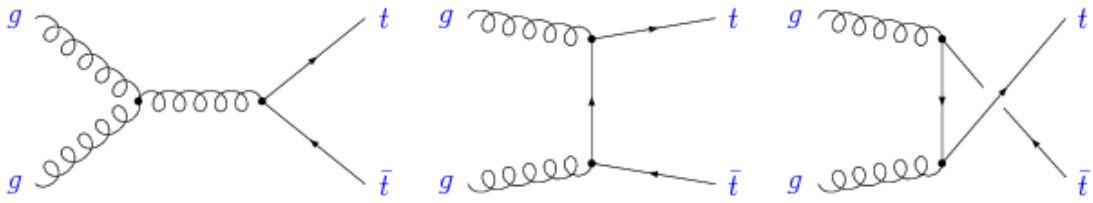

Figure 2.2: *Feynman diagrams for the $t\bar{t}$ production with gluons. The graphic is taken from Ref. [12].*

The most probable way to produce a top-quark at the LHC is via the production of a $t\bar{t}$ pair. Dominant Feynman diagrams of this process are shown in Figure 2.2. In the diagrams shown, two gluons form the initial state. That is why this process is called gluon-gluon fusion. In Figure 2.3 the parton distribution function (PDF) of a proton, is shown. A PDF describes the probability for a parton, to take a certain energy fraction [13],[14]. The PDF is the reason, why it is more probable to generate a $t\bar{t}$-pair via two gluons then via quark-antiquark annihilation. This is due to the fact, that the center-of-mass energy of 13 TeV is much higher than the invariant mass of the $t\bar{t}$ pair. Therefore, only a small momentum fraction of the initial partons is required to produce a top-quark-antiquark pair. But in this regime there is a much larger probability to have a gluon than an antiquark. This is why the gluon fusion is the dominant process.

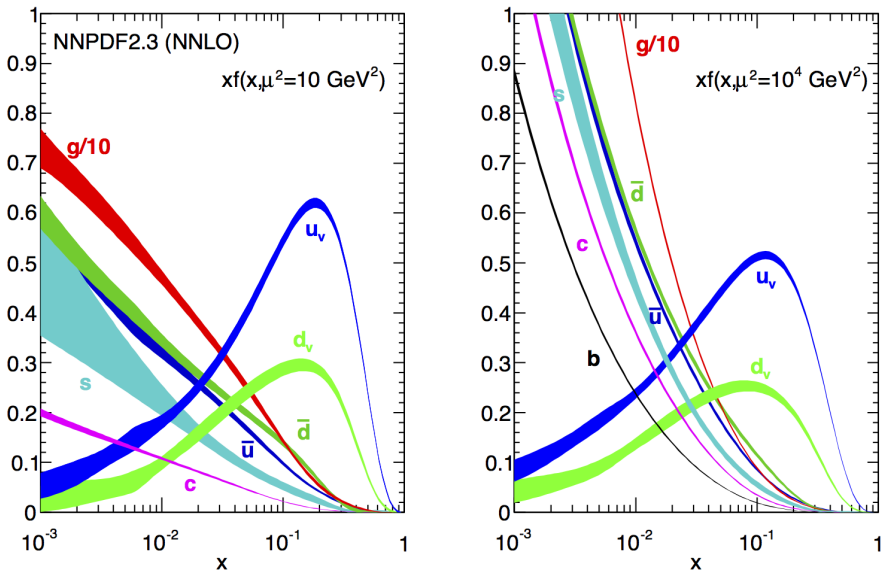

Figure 2.3: *Parton distribution functions of the proton at the energy scale $Q^2 = 10\ GeV^2$ and $Q^2 = 10^4\ GeV^2$. The graphic is taken from Ref. [15].*

2.3 Single top-quark

While $t\bar{t}$ pairs are produced via the strong force, there is also the possibility to produce single top-quarks via the weak force.

Exemplary Feynman diagrams are shown in figure 2.4 for the dominant t-channel single top-quark production (a), the associated production of a top quark and a W-boson, called the Wt-channel (b) and the s-channel process (c).

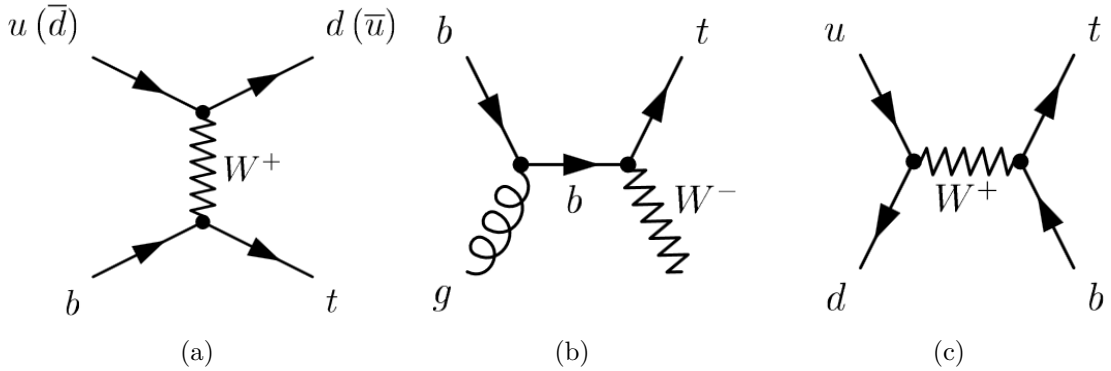

Figure 2.4: *Feynman diagrams of single-top (a) t-channel, (b) associated Wt, and (c) s-channel production. The graphic is taken from Ref. [16]*

Since the lifetime of the top quark is that short, it can not be detected directly with a detector. Instead the decay products are measured, thus the top quark has to be reconstructed. Because of the high value of $V_{tb} \approx 1$ the top quark decays with a probability of nearly 100% into a W-boson and a bottom-quark. The lifetime of the W-boson is also very short, therefore it decays, before it is detected. In this thesis only those events are considered, where the W-boson decays leptonically into a charged lepton, an electron or a muon, and the corresponding neutrino. So the particles reconstructed within the detector are: one electron or muon, one light quark, detected as a jet of many particles pointing in one direction, and one b-tagged jet, originating from a bottom-quark. Also the neutrino can be reconstructed by using the missing transverse momentum.

2.4 Background processes

The same particles can be created in different processes and therefore these reactions have to be considered, too. One of these so called background processes with a large contribution to the single top-quark background is the already described $t\bar{t}$ production. If one of the b-jets, originating from the top quark decays, is not identified as a b-jet and two of the light jets are not identified as jets, the $t\bar{t}$-production can have the same signature as the single top-quark production. Since the cross-section of this background is ≈ 10 times larger (figure 2.6), than the signal-process cross-section, the $t\bar{t}$-production is one of the dominant background processes. Also the other single-top production channels are backgrounds of the t-channel. The Feynman diagrams of the top processes are shown in figure 2.5.

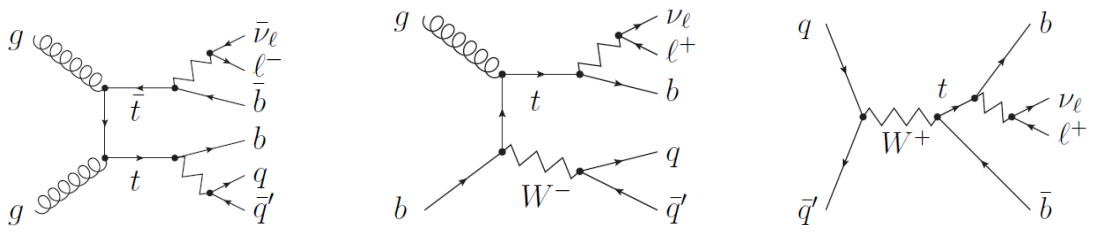

Figure 2.5: *Feynman diagrams of the top-quark background processes. The $t\bar{t}$ process with semi-leptonic decay (a), the associated Wt production (b), and the single top-quark s-channel production (c). The graphic is taken from Ref. [17]*

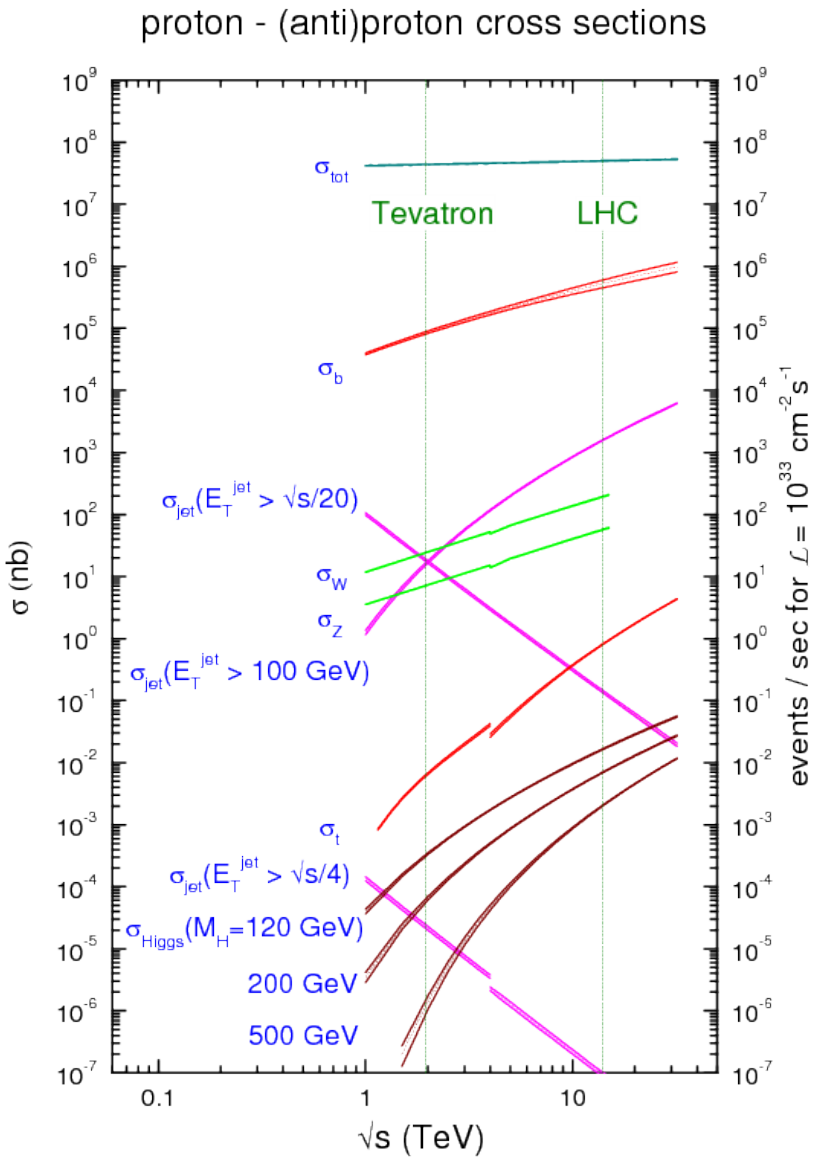

Figure 2.6: *Cross sections of different processes for different center of mass energies. The graphic is taken from Ref. [18]*

The other dominant background process is the W+jets process, for which a corresponding Feynman graph is shown in Figure 2.7(a). In such a process the W-boson decays leptonically into an electron or muon and the corresponding neutrino. Additionally, jets are produced. As shown in Figure 2.6, the cross section for W+jets events is large.

Figure 2.7: *Feynman diagrams of the W+jets (a) and the multijet (b) background. The graphic is taken from Ref. [17]*

One smaller background processes is the multijet background. Since the LHC is a proton-proton collider, there are many multijet events produced in quantum-chromodynamic interactions. If one of the jets, produced in a multijet event, is incorrectly identified as a lepton, the event can look like a single top-quark event, since there can always be missing transverse momentum by the uncertainty of its measurement. A Feynman graph for such a process is shown in figure 2.7(b). The probability for a misidentification is very low, but since the production cross section is very big, multijet events have to be taken into account for this analysis.

Another contribution that is taken into account are the Z+jets and diboson backgrounds. The corresponding Feynman diagrams are shown in Figure 2.8. The Z+jets process is very similar to the W+jets process. The difference is, that the Z-boson decays into two leptons (electrons or muons). If one of the leptons is not detected as a lepton, the process is identified as a signal process. Since one lepton has to be lost, this process is a smaller background than the W+jets process. In the diboson background either two W-bosons, two Z-bosons, or one W-boson and one Z-boson are produced. To identify a diboson process as a signal, one boson decays leptonically, to produce an electron or a muon and the other one hadronically, to produce the jets. Since this process is rare, the diboson process is also a small background for the analyzed single top-quark process.

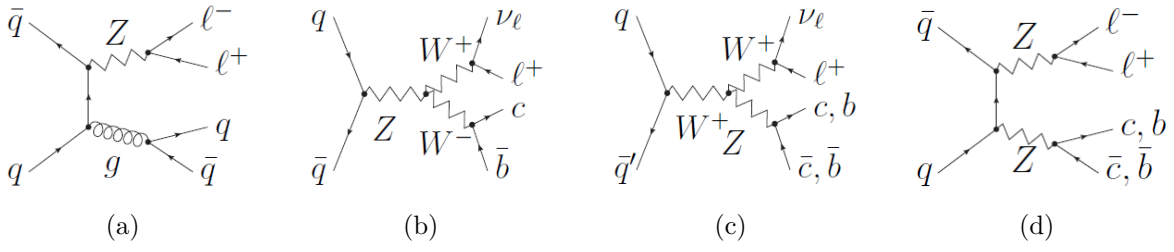

Figure 2.8: *Feynman diagrams of the Z+jets (a) and the diboson backgrounds. For the diboson processes, a WW (b), a WZ (c) and a ZZ (d) diagram is shown. The graphic is taken from Ref. [17]*

3 LHC and the ATLAS Detector

Because of their high mass, high energies are necessary to produce top-quarks. These energies are reached in large accelerators, which accelerate elementary or bound state particles to collide them. In these collisions high energies are released, so that heavy particles can be produced. The accelerator, that has currently the highest center-of-mass energy is the Large Hadron Collider (LHC) located at the European Organization for Nuclear Research (CERN) in Geneva. The particles, produced in such collisions, are measured with detectors. This chapter contains a description of the LHC accelerator complex and the ATLAS detector, which was used to collect the data presented in this thesis.

3.1 Large Hadron Collider

The LHC is currently the largest particle accelerator in the world. It is a synchrotron, with a design center-of-mass energy of 14 TeV. In the beam lines, protons or heavy ions are accelerated in both directions to collide them at four interaction points. At each interaction point there is one large detector, to detect particles, produced in the collisions. There are two multi-purpose detectors, the ATLAS and the CMS (Compact Muon Solenoid) detector, both constructed to search for new physics in many channels and high precision measurements of the SM. The ALICE (A Large Ion Collider Experiment) detector is build to measure especially ion collisions and the LHCb (Large Hadron Collider beauty) is a fixed-target experiment to measure mainly processes involving bottom-quarks with very high precision.

The injected protons or heavy ions are accelerated not just in the LHC, but in many pre-accelerators. A scheme of the CERN accelerators is shown in 3.1. To obtain protons for the beam an electric field is used to extract protons of hydrogen gas. The protons are accelerated in a first step in the LINAC2, a linear accelerator, to an energy of 50 MeV. The first ring accelerator is the Proton Synchrotron Booster, which accelerates the protons to an energy of 1.4 GeV. In the Proton Synchrotron (PS) the protons are further accelerated to 25 GeV. The last pre-acceleration up to an energy of 450 GeV is done in the Super Proton Synchrotron (SPS). After the pre-acceleration the proton-bunches are divided in two halves, where each of them is headed in one direction of the LHC, to accelerate them to a design energy of 7 TeV per beam.

Each acceleration is done with a alternating voltage. There are certain areas equipped with cavities to which an alternating electric field is applied. In these cavities the protons are accelerated. The timing of the proton bunches is such that the particles travel on the increasing or decreasing edge of the alternating voltage for relativistic or classical particles, respectively. Since no continuous beam can be accelerated like this, the protons are formed to bunches. Through the acceleration frequency of 400.8 MHz the LHC has 35640 radio frequency (RF) buckets in each beam, where a proton bunch can be placed. But not all of the buckets are filled with bunches, since the interaction of two bunches with each other and with the accelerator destabilizes the beams.

The number of interactions per area and time is measured with the luminosity. Often the integrated luminosity $\mathcal{L}_{\text{int}}$ is used, which is the luminosity integrated over a certain time [19]. With the integrated luminosity the estimated number of events can be calculated:

$$N = \epsilon \sigma \mathcal{L}_{\text{int}} \tag{3.1}$$

Here N is the number of observed events, and σ is the cross section. ϵ is the efficiency of detecting an event with the detector and passing all the selection criteria.

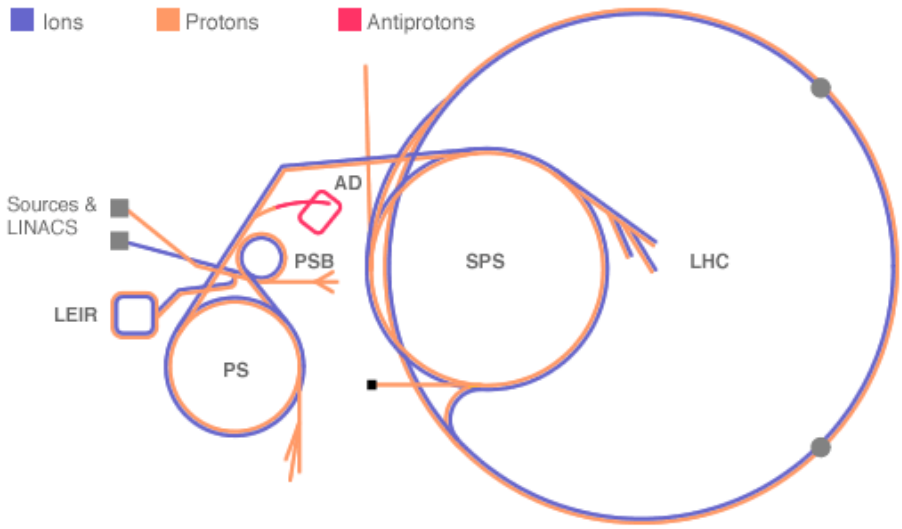

Figure 3.1: *Schema of the different accelerators at CERN. The graphic is taken from Ref. [20].*

3.2 The ATLAS Detector

In this thesis data taken with the ATLAS detector are analyzed [21]. The ATLAS detector, shown in figure 3.2 is a multi-purpose detector located at the LHC. It has a diameter of 25 m, a length of 46 m and weighs about 7000 tons. It has a cylindrical form and is placed around the beam pipe. In the middle of the detector is the interaction point, where the proton-bunches collide. The resulting particles are scattered around the interaction point and then measured by the ATLAS detector. The ATLAS detector consists of different subdetectors, which have also a cylindrical form and are arranged in radial distances to the beam pipe. The most inner subdetector is the so-called Inner Detector (ID) and consists of the Pixel Detector, the Semiconductor Tracker and the Transition Radiation Tracker. Its purpose is to detect the position of the charged particles, produced in the collision. To also detect the charge and momentum, the Inner Detector is surrounded by a solenoid magnet, that creates a magnetic field in beam direction. The next subdetectors are the calorimeters. Their purpose is to measure the energy and direction of electrons, photons and jets and to distinguish them. Electrons and photons are absorbed in the electromagnetic calorimeters. The hadronic part of a jet does not interact so strongly with the electromagnetic calorimeters and is absorbed afterwards in the hadronic calorimeters. The most outer subdetector is the Muon Spectrometer, consisting of muon chambers. Muons don't interact that much with the detector, so they can cross all the inner detectors without loosing much energy. A magnetic field is provided by the toroid magnets, to measure their momenta. Neutrinos don't interact with the detector and so can't be measured directly. But with the assumption, that there was no transverse momentum before the collision and momentum conservation, the transverse momentum of one neutrino can be calculated, by summing up all the measured transverse momenta.

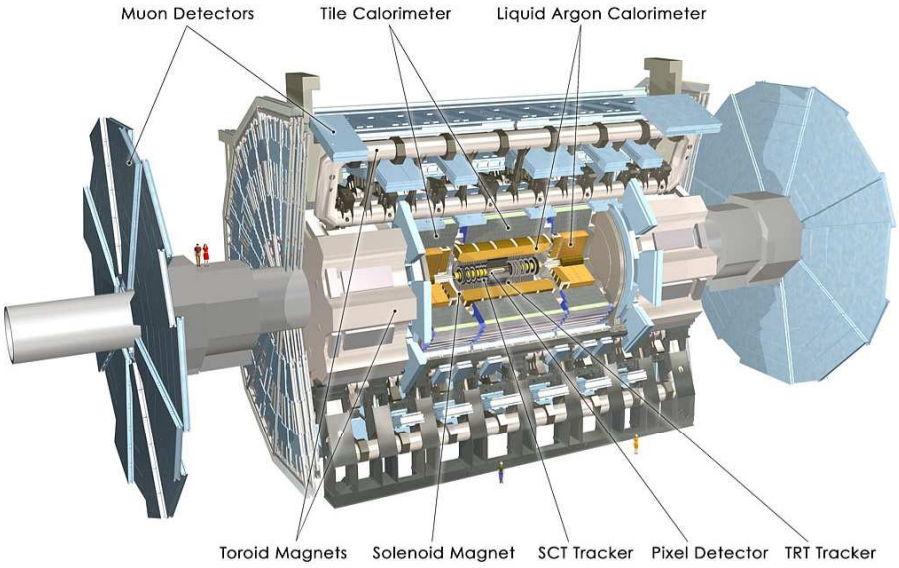

Figure 3.2: *Schema of the ATLAS detector. The graphic is taken from Ref. [22].*

3.3 The coordinate system

The coordinate system of the ATLAS detector is arranged around the beam pipe. Because of the form of the detector, cylindrical coordinates are used, where the origin is located at the interaction point. The z-component is pointing in the direction of the beam pipe. The azimuthal angle Φ measured from $-\pi$ to π around the beam pipe, where $\Phi = 0$ is pointing to the center of LHC. The polar angle θ is the angle measured from the positive z-axis. Often the rapidity

$$y = \frac{1}{2} \ln \left(\frac{E + p_z}{E - p_z} \right) \tag{3.2}$$

with the energy E of the particle and the z-component of the momentum p_z is used to describe the angle instead of θ. In this thesis the pseudorapidity is used, which is an approximation for the rapidity for particles with a small mass compared to their energy, $m \ll E$, and defined as

$$\eta = -\ln \left(\tan \frac{\theta}{2} \right). \tag{3.3}$$

With this definition the distance ΔR between two objects is defined in the pseudorapidity-azimuthal angle space as

$$\Delta R = \sqrt{\Delta\eta^2 + \Delta\Phi}\,. \tag{3.4}$$

With

$$\Delta\eta = |\eta_1 - \eta_2| \quad , \quad \Delta\Phi = |\Phi_1 - \Phi_2| \tag{3.5}$$

Often the transverse momentum $\vec{p_{\mathrm{T}}}$ is considered, because the vectorial sum over the transverse momenta of all produced particles should be 0, since the initial transverse momentum is 0 and conserved. The absolute value of the transverse momentum is defined as

$$p_{\mathrm{T}} = \sin(\theta) \cdot |\vec{p}|\,. \tag{3.6}$$

With the transverse momentum the variable H_{T} can be defined as the sum of the absolute values of p_{T} of all particles (jets, charged leptons and missing transverse momentum)

$$H_{\mathrm{T}} = \sum_i \left|p_{\mathrm{T}}^i\right| \tag{3.7}$$

3.4 Dataset of this analysis

This analysis uses the data taken with the ATLAS detector at the LHC from 4th June till 16th July 2015 at $\sqrt{s} = 13$ TeV with 50 ns spaces between two bunches. In Run 1, the LHC collided protons till end of 2012 with an energy of $\sqrt{s} = 8$ TeV. In a shut-down time in 2013 and 2014 the LHC and the detectors were updated to deal with higher energies and luminosities. In 2015, the LHC started cycling proton beams with a center-of-mass energy of 13 TeV marking the beginning of Run 2. First collisions were produced and recorded by the ATLAS detector in June. In Figure 3.3 the integrated luminosity from the beginning of data taking to end of August is shown. This analysis uses data taken till the 16th of July, which corresponds to an integrated luminosity of 85 pb^{-1}. The integrated luminosity shown in Figure 3.3 is slightly higher. This is because in the plot all the data collected with the ATLAS detector is shown, even if not all the subdetectors were operational and ready to take data. Since this analysis uses all types of reconstructed particles, except photons not all of the collected data can be used. The runs and luminosity blocks, for which all the subdetectors were switched on and the detector worked correctly are listed in so called good run lists (GRL). Table 3.1 shows a list of the used runs together with their peak and integrated luminosity.

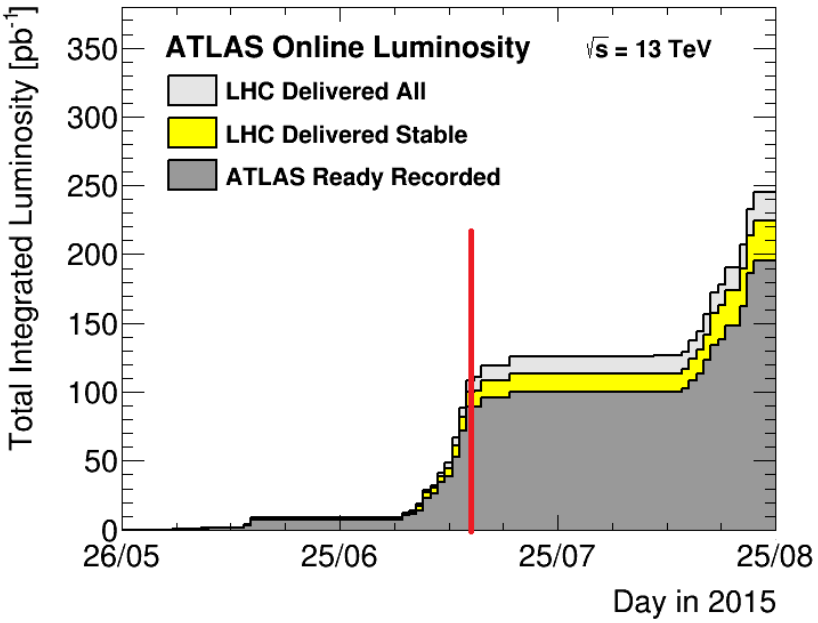

Figure 3.3: *Integrated luminosity delivered by LHC and recorded by ATLAS from June till August 2015. The graphic is taken from Ref. [23].*

Table 3.1: *List of runs used in this analysis. Also the peak and integrated luminosity for each run is listed [23].*

run number	bunches colliding	peak stable luminosity $[10^{32}\mathrm{cm}^{-2}\mathrm{s}^{-1}]$	$\mathcal{L}_{\mathrm{int}}$ $[\mathrm{pb}^{-1}]$
267073	2	0.0551	0.086
267167	6	0.2310	0.225
267358	34	0.000135	0.000
267359	37	0.000323	0.000
267360	11	0.00467	0.000
267367	37	0.00210	0.002
267385	37	0.00217	0.006
267599	29	0.00178	0.006
267638	38	1.2400	3.373
267639	38	1.3500	2.983
270806	110	3.2100	0.776
270953	110	2.7700	4.586
271048	110	3.1100	6.734
271298	254	6.0400	9.970
271421	254	9.7700	13.610
271516	414	13.2000	19.723
271595	414	16.0000	16.594
271744	256	9.3900	6.293
		total	84.968

4 Monte Carlo generators

In proton-proton collisions like at the LHC many different particles are produced nearly at the same time. Many of them produce signals in the detector, which superimpose with signals from a studied process. To predict all of the signals, recorded by the detector, Monte Carlo (MC) simulations are used. The MC simulation can be divided into several steps. In a first step the interaction of two protons is considered, and the production of particles with their kinematics, according to the SM prediction, is simulated. This is done by a program called event generator. Then the interaction of those particles with the detector is simulated to get a prediction for the detector signals. Those signals are reconstructed in the same way as the measured data. Finally, the measured and simulated events can be compared.

4.1 Particle collisions

In Figure 4.1 a typical particle collision of two protons is shown. The interactions occurring as part of the collision can be divided into three different types. The first important property is, that in collisions with high energies, like at the LHC, the colliding particles are not the protons, but their partons, the quarks and gluons. Therefore, the examined process, the hard process, is a collision of two or more partons. The remaining partons have two interact, too, because they carry a color charge and so can not exist separately. These interactions are called underlying event and produce additional particles, which are detected in the detector. More signals are produced by the so called pile-up. The pile-up is produced via other protons of the colliding bunches, which interact at the same time.

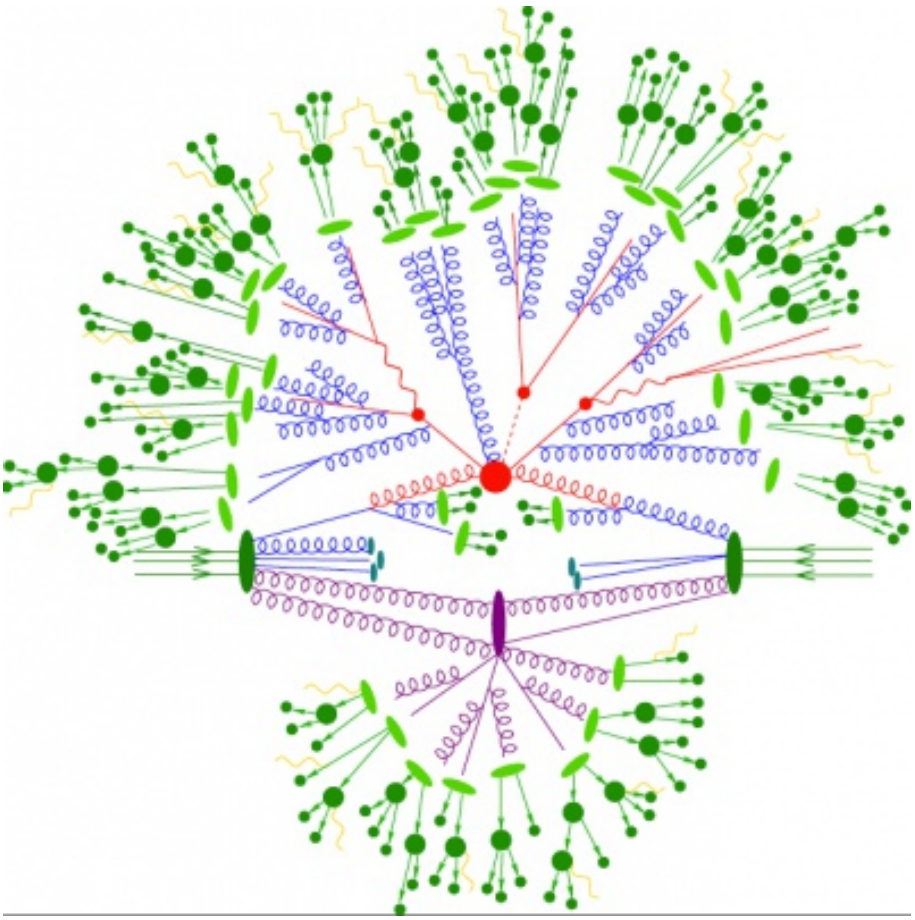

Figure 4.1: *Schema of a proton-proton collision. Shown are the different types of interactions occurring in a single proton-proton collision. The graphic is taken from Ref. [24].*

The hard process can be again divided into steps. The first step is the interaction of the partons of the protons, which can be calculated theoretically and simulated by MC generators. The result of these simulations are elementary particles, that can carry a color charge. In the next step, the so called shower development happens, where the particles originating from the hard process cause a shower of secondary particles. In this so called parton shower gluons are emitted and splitting of gluons in quark-antiquark pairs occurs. At the end of the shower development the single partons have energies low enough to form bound states, i.e. hadrons. This formation is called hadronisation. In a last step the decay of the hadrons takes place. The result are the particles, that can be measured by a detector.

4.2 Monte-Carlo generators

There are two types of Monte-Carlo generators, the multi-purpose (MP) generators and the matrix-element (ME) generators. The MP generators are able to simulate the whole interaction, that is the hard process, the showering, the hadronisation, and particle decays. Alternatively, the simulation of the hard process can be done by ME generators. These are use to generate the final state of the hard process and to calculate its cross section. Since ME generators can't simulate the showering they have to be used in combination with a MP generator. This combination is not trivial, because radiation of jets for example can occur in the hard process or in the showering. To avoid double counting a matching between the partons of the parton shower and the hard-process final-state partons is done. In the following different ME and MP generators are described.

- **Powheg** [25],[26] The Powheg-Box is a ME generator, that performs ME calculations at NLO accuracy. It has the feature to generate only positive weighted events, using exact NLO matrix elements. In this analysis Powheg is used for ME calculation of the $t\bar{t}$, the Wt- and the single top-quark t-channel samples.

- **Pythia** [27] Pythia is an MP generator, that can be used to compute all steps of the simulation. The program does ME calculations at LO and uses a string model for hadronisation. It is also able to simulate multiple interactions. In this analysis Pythia is only used in combination with Powheg for the ME calculations. This analysis uses Pythia to simulate the shower development for the top-quark processes generated with Powheg.

- **Herwig++** [28] Herwig++ is an MP generator able to simulate all interactions, except the underlying event. It uses a parton-shower approach for QCD-radiation. For hadronisation a cluster model is implemented.

- **Sherpa** [29] Sherpa is an MP generator. It computes ME calculations at LO accuracy. The emission of QCD partons is done by parton showers in the initial and final state. The shower development is implemented with a cluster-hadronisation model. Also a simple model of multiple interactions for the underlying event is implemented. This analysis uses Sherpa for W+jets, Z+jets and diboson samples. The W+jets and Z+jets samples are sliced into p_{T} ranges of the boson.

- **Madgraph5_aMC@NLO** [30] Madgraph5_aMC@NLO is a ME generator, that computes ME calculations at LO accuracy. QCD corrections can be done to NLO accuracy. Also methods for parton-shower simulation matching are provided.

4.3 Monte-Carlo samples

In this analysis several MC samples are used. A list of all available samples can be found at [31]. Samples, containing top-quarks, generated with Powheg and Pythia are listed in table 4.1. The used diboson samples are generated with Sherpa and listed in table 4.2. For the W+jets (Table 4.3) and Z+jets (Table 4.4) processes Sherpa samples are used. The samples are sliced into ranges of p_{T} of the corresponding boson. There is also the cross section σ times branching ratio $\mathcal{B}$ listed in the tables. The branching ratio provides the probability of a certain decay mode.

Table 4.1: *List of used samples generated with Powheg and Pythia. Also $\sigma \times \mathcal{B}$ is listed.*

process	Dataset number	$\sigma \times \mathcal{B}$ [pb]
$t\bar{t}$ non-allhad	410000	451.7
top-quark (t-channel) $W \to l\nu$	410011	43.7
top-antiquark (t-channel) $W \to l\nu$	410012	25.8
top-quark (Wt-channel) $W \to l\nu$	410013	34.0
top-antiquark (Wt-channel) $W \to l\nu$	410014	34.0

Table 4.2: *List of used diboson samples generated with Sherpa. Also $\sigma \times \mathcal{B}$ is listed.*

process	Dataset number	$\sigma \times \mathcal{B}$ [pb]
$Z + Z \to ll + ll$	361063	12.6
$Z + Z \to ll + \nu\nu$	361068	14.0
$W + W \to l^{+}\nu + qq$	361081	26.0
$W + W \to l^{-}\nu + qq$	361082	26.0
$W + Z \to l\nu + qq$	361083	12.5
$W + Z \to qq + l\nu$	361084	3.8
$W + Z \to qq + \nu\nu$	361085	7.4
$Z + Z \to qq + ll$	361086	2.3
$Z + Z \to qq + \nu\nu$	361087	4.6

Table 4.3: *List of used W+jets samples generated with Sherpa. Also $\sigma \times \mathcal{B}$ is listed.*

process	Dataset number	p_{T} range [GeV]	filter	$\sigma \times \mathcal{B}$ [pb]
$W \to e\nu$	361300	0-70	light-jets	17216
$W \to e\nu$	361301	0-70	c-Filter	957
$W \to e\nu$	361302	0-70	b-Filter	1161
$W \to e\nu$	361303	70-140	light-jets	419
$W \to e\nu$	361304	70-140	c-Filter	101
$W \to e\nu$	361305	70-140	b-Filter	55
$W \to e\nu$	361306	140-280	light-jets	56
$W \to e\nu$	361307	140-280	c-Filter	17
$W \to e\nu$	361308	140-280	b-Filter	9
$W \to \mu\nu$	361324	0-70	light-jets	17340
$W \to \mu\nu$	361325	0-70	c-Filter	919
$W \to \mu\nu$	361326	0-70	b-Filter	1159
$W \to \mu\nu$	361327	70-140	light-jets	420
$W \to \mu\nu$	361328	70-140	c-Filter	100
$W \to \mu\nu$	361329	70-140	b-Filter	56
$W \to \mu\nu$	361330	140-280	light-jets	56
$W \to \mu\nu$	361331	140-280	c-Filter	17
$W \to \mu\nu$	361332	140-280	b-Filter	9
$W \to \tau\nu$	361348	0-70	light-jets	17314
$W \to \tau\nu$	361349	0-70	c-Filter	946
$W \to \tau\nu$	361350	0-70	b-Filter	1159
$W \to \tau\nu$	361351	70-140	light-jets	416
$W \to \tau\nu$	361352	70-140	c-Filter	102
$W \to \tau\nu$	361353	70-140	b-Filter	55
$W \to \tau\nu$	361354	140-280	light-jets	56
$W \to \tau\nu$	361355	140-280	c-Filter	17
$W \to \tau\nu$	361356	140-280	b-Filter	9

Table 4.4: *List of used Z+jets samples generated with Sherpa. Also $\sigma \times \mathcal{B}$ is listed.*

process	Dataset number	p_{T} range	filter	$\sigma \times \mathcal{B}$ [pb]
$Z \to ee$	361372	0-70	light-jets	1549
$Z \to ee$	361373	0-70	c-Filter	283
$Z \to ee$	361374	0-70	b-Filter	158
$Z \to ee$	361375	70-140	light-jets	44
$Z \to ee$	361376	70-140	c-Filter	15
$Z \to ee$	361377	70-140	b-Filter	9
$Z \to ee$	361378	140-280	light-jets	7
$Z \to ee$	361379	140-280	c-Filter	3
$Z \to ee$	361380	140-280	b-Filter	2
$Z \to \mu\mu$	361396	0-70	light-jets	1547
$Z \to \mu\mu$	361397	0-70	c-Filter	282
$Z \to \mu\mu$	361398	0-70	b-Filter	158
$Z \to \mu\mu$	361399	70-140	light-jets	44
$Z \to \mu\mu$	361400	70-140	c-Filter	15
$Z \to \mu\mu$	361401	70-140	b-Filter	9
$Z \to \mu\mu$	361402	140-280	light-jets	6
$Z \to \mu\mu$	361403	140-280	c-Filter	3
$Z \to \mu\mu$	361404	140-280	b-Filter	2
$Z \to \tau\tau$	361420	0-70	light-jets	1540
$Z \to \tau\tau$	361421	0-70	c-Filter	283
$Z \to \tau\tau$	361422	0-70	b-Filter	157
$Z \to \tau\tau$	361423	70-140	light-jets	45
$Z \to \tau\tau$	361424	70-140	c-Filter	15
$Z \to \tau\tau$	361425	70-140	b-Filter	9
$Z \to \tau\tau$	361426	140-280	light-jets	6
$Z \to \tau\tau$	361427	140-280	c-Filter	3
$Z \to \tau\tau$	361428	140-280	b-Filter	1

5 Object reconstruction and event selection

In the reconstruction, signals of the detector are used to reconstruct physics objects. For this purpose all subdetectors are used to check certain criteria that the reconstructed objects have to fulfill. In this chapter the reconstruction techniques used in the ATLAS detector are summarized and the event selection used in this analysis is provided.

5.1 Tracking

Charged particles generate charged tracks, which form a helix in the magnetic field. Tracks are reconstructed using the signals of the Inner Detector. This can be very challenging, because there are many particles produced in the collisions, which place a signal in the Inner Detector. Two methods are used to reconstruct the tracks. The basis of both is the transformation of the electrical signals into space-points. In the first method, the inside-out method [32], the start points are at the innermost detector, the pixel detector. For each space-point, reconstructed from a electrical signal, an algorithm is used to combine the space-point with others in outer layers and to form track seeds. These tracks are fitted and the compatibility of other space points with this track is analyzed with a Kalman filter [33] [34].

The second method, the outside-in method, which is used in addition after the inside-out method is evaluated. It uses the same procedure, but the starting points are unused signals in the outermost layer of the tracking detector. From there tracks are reconstructed to the inside. This procedure improves especially the tracking efficiency of tracks with vertices outside the innermost detector, like tracks from long-lived particles.

5.2 Vertex reconstruction

For precise particle measurement, the location of vertices, especially of the hard process, has to be known. To find the vertices an iterative vertex finding approach

is used [35]. The first step of this approach is to pre-select all the tracks that could be originating from the interaction region. The global maximum of the z-coordinates of these tracks is used to obtain a vertex seed. The tracks and the seeds are then fitted with a χ^2-fit, to determine the position of the vertex. Tracks that are incompatible with the vertex by more than 7σ are used to create a new vertex seed. In the next step, both vertices are fitted simultaneously. This procedure is repeated until all tracks are associate with a vertex.

5.3 Charged lepton reconstruction

To detect an electron candidate [36] a signal of at least 2.5 GeV of transverse energy deposition in the electromagnetic calorimeter is required. The energy should be deposited in a cluster of 3×5 in units of 0.025×0.025 in the (η, Φ) space. Then tracks candidates with $p_T < 500$ MeV are refitted to originate from an electron. A track matches to the electromagnetic cluster, if $|\Delta\eta| < 0.05$. There are three categories in which electron candidates are grouped: *loose*, *medium* and *tight*. For each of the groups a candidate has to fulfill different criteria, where the criteria from each group to another gets stronger. So all of the candidates belonging to the *tight* group also fulfill the *medium* criteria. The effect of the stronger criteria is, that the purity in the *tight* group is the highest, but the efficiency is the lowest of the groups.

Muons are reconstructed using the Muon Spectrometer [37]. Therefore different track segments are combined to get a full track that is required to point loosely to the interaction point. Additionally information of the calorimeters and the Inner Detector can be used to fulfill different kind of criteria for muon candidates.

5.4 Jet reconstruction

Jets are clusters of many particles, produced from one high energetic colored partons. To reconstruct these partons, the jet has to be measured precisely [38]. The identification of a jet is done in the calorimeters, where the deposited energy in adjacent cells is measured. This energy is used as a starting point for the following jet-finding algorithm. ATLAS uses the anti-k_t algorithm to sequentially recombine soft and hard particles. Soft particles are preferentially combined with hard ones, than with each other. Therefore the area of the jet is determined by the hard particles. Finally, the four-momentum of the jet has to be corrected, to take care of inefficiencies of the detector, the composition of the shower and pile-up events.

5.5 Missing transverse momentum

In a proton-proton collision the initial four-vector of the interacting partons is not known. The only assumption is, that the transverse momenta of the partons can be neglected, compared to the total energy, so that $\vec{p}_{\mathrm{T}}^{\,\mathrm{initial}} = 0$. With the assumption of momentum conservation the final transverse momentum of all particles should also be zero again. A larger difference $E_{\mathrm{T}}^{\mathrm{miss}}$ can be measured, if particles are produced, that can't be measured by the detector, like neutrinos. The missing transverse momentum is defined as

$$E_{\mathrm{T}}^{\mathrm{miss}} = \sqrt{(E_{\mathrm{x}}^{\mathrm{miss}})^2 + \left(E_{\mathrm{y}}^{\mathrm{miss}}\right)^2} \tag{5.1}$$

and is the sum of energies detected in the calorimeter and the muon system. The reconstruction is explained in Ref. [39].

6 Background modeling

As discussed in chapter 2.4, the t-channel single-top analysis has to deal with many background processes. In order to get a precise result for the single top-quark cross-section, a good knowledge of all the backgrounds is necessary. In this chapter the method to obtain the multijet-background is explained and a control region (CR) for the W+jets background is introduced.

6.1 Multijet background estimation

The multijet background is different compared to all other examined processes. The difference is that there is no isolated lepton in the final state of a multijet event. Therefore a jet has to be misidentified as a lepton, which is very rare, so that a multijet event has the same signature as a single top-quark event. But the large amount of QCD interactions, that produce multijet events, in the LHC compensates this small probability, leading to a significant number of events, that must be taken into account. Because of these properties of multijet-events it is not practical, to simulate them with a reasonable statistics, like the other processes. In ATLAS there are different methods used to get multijet background in electron and muon channels.

For electrons, this analysis uses the jet-lepton model [40]. This methods identifies jets, that have similar properties like electrons, as electrons. To generate a multijet sample, a dijet Monte-Carlo sample is used, where all the signal selection cuts are applied, except the required electron identification. If a jet has a fraction of its deposited energy in the electromagnetic calorimeters between 80% and 95% the jet is called a jet-lepton candidate. If there are more than one candidates, the one with the higher energy fraction in the electromagnetic calorimeter is chosen.

For muons, this analysis uses the anti-muon model [41], which selects muons, that could originate from a jet. To generate such a sample, data samples, enriched in muons are used. To select muons, originating from jets instead of the hard process, some selection cuts are relaxed or inverted. Thus, isolation criteria are relaxed and an energy deposit in the electromagnetic calorimeter in a cone of $dR < 0.2$ around the muon track larger than 0.03 of $p_{\mathrm{T}}(\mu)$ is required. This analysis uses

multijet samples, which were produced for the 8 TeV analysis at 8 TeV. As the figures in this chapter show, the used samples are suitable for the 13 TeV studies as well.

To get the amount of multijet events a binned maximum-likelihood fit is used in this thesis. After applying all selection criteria, except for the $m_{\mathrm{T}}(W)$ cut, the processes are fitted to the observed data in the $m_{\mathrm{T}}(W)$ distribution. For this the electron channel is divided in one end-cap region for electrons with $|\eta| > 2.5$ and one barrel region with $|\eta| < 2.5$. Thus the multijet background is fitted in two electron and one muon channel separately. For the fit all top processes are added to one template with one scale value. The amount of the Z+jets and diboson events is fixed, due to their small contribution. Constraints are set of the top (10%) and W+jets (20%) processes according to their theoretical prediction. The fitted distributions are shown for each fitted channel in the SR in Figure 6.1 and the CR in Figure 6.2, introduced in following chapter 6.2. From the fit result the amount of multijet events after applying the $m_{\mathrm{T}}(W)$ cut is calculated. In table 6.1 the estimated event fraction of multijet events after applying additionally the $m_{\mathrm{T}}(W)$ cut is listed for the SR and the CR.

Table 6.1: *Estimated event fraction of multijet events after applying additionally the $m_T(W)$ cut.*

Channel	Control region	Signal region
barrel electron	29.8 %	20.0 %
end-cap electron	30.4 %	27.2 %
muon	8.4 %	11.3 %

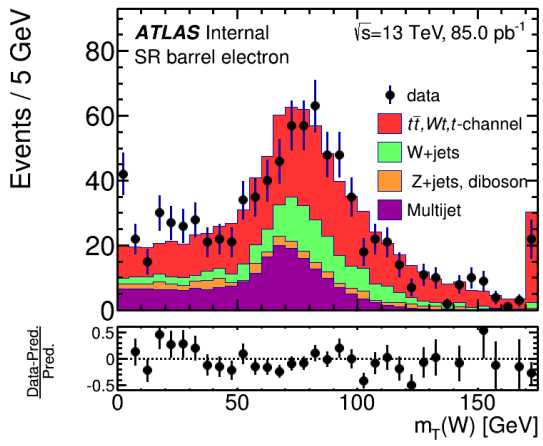

(a)

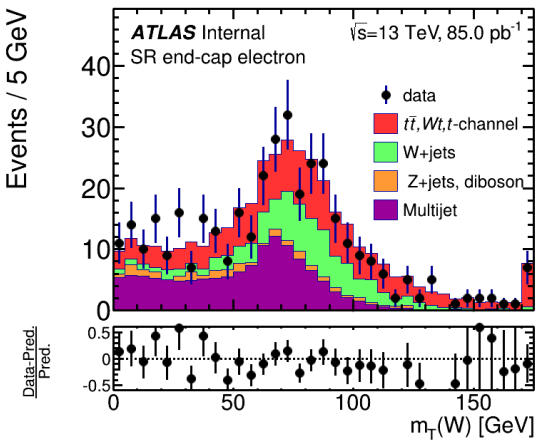

(b)

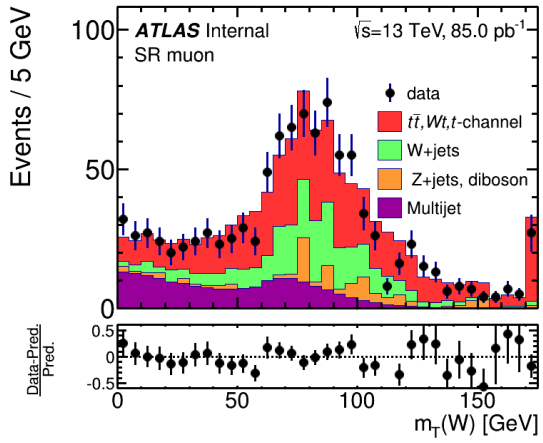

(c)

Figure 6.1: *Shown are the $m_T(W)$ distributions after the QCD fit for all channels in the SR. In the lower panels the relative difference between MC events and observed data is shown for each bin.*

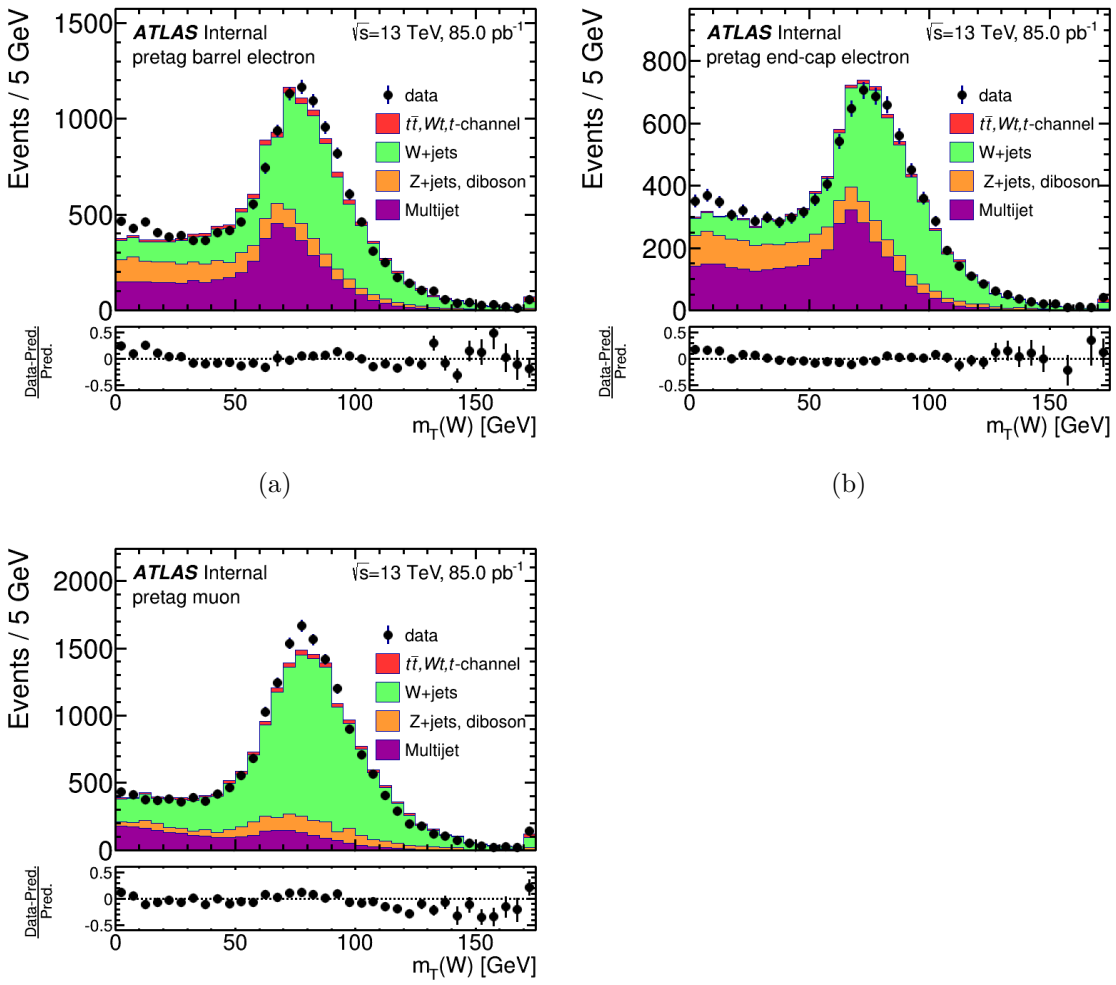

Figure 6.2: *Shown are the $m_T(W)$ distributions after the binned maximum-likelihood fit in the $m_T(W)$ distribution for all channels in the CR. In the lower panels the relative difference between MC events and observed data is shown for each bin.*

6.2 W+jets control region

To get a precise measurement of the signal process, a good knowledge of the background processes is necessary. A method to check the different backgrounds is the introduction of control regions, where no or not much signal is expected and that is ideally dominated by one of the background processes. As described in chapter 2.3 this analysis aims to extract the t-channel single top-quark cross-section in the lepton+jets-channel. Therefore, the signature is one charged lepton (electron or

muon), missing transverse momentum and exactly two jets, where exactly one of them is b-tagged. In order to get a CR with less single-top events, the requirement of the b-tagged jets is skipped. In this so called pretag-region events are therefore selected with one charged lepton, missing transverse momentum and exactly two jets. This CR is dominated by W+jets events. Also Z+jets and multijet processes are present in this CR. In Figure 6.3 and 6.4 kinematic variables of the reconstructed particles are shown. The estimated number of events is normalized to the binned maximum-likelihood fit in the $m_{\mathrm{T}}(W)$ distribution, as described in chapter 6.1. Here jet1 is the jet with higher transverse momentum and jet2 is the jet with lower transverse momentum.

In general the MC distributions agree with the data. But especially for the jets, there are some disagreements. In the regions for high values of the pseudo rapidity and for low transverse momenta there are more events expected than detected. The reason for this disagreement can be the preliminary calibration. Also for electrons there are more events expected than detected for low transverse momenta.

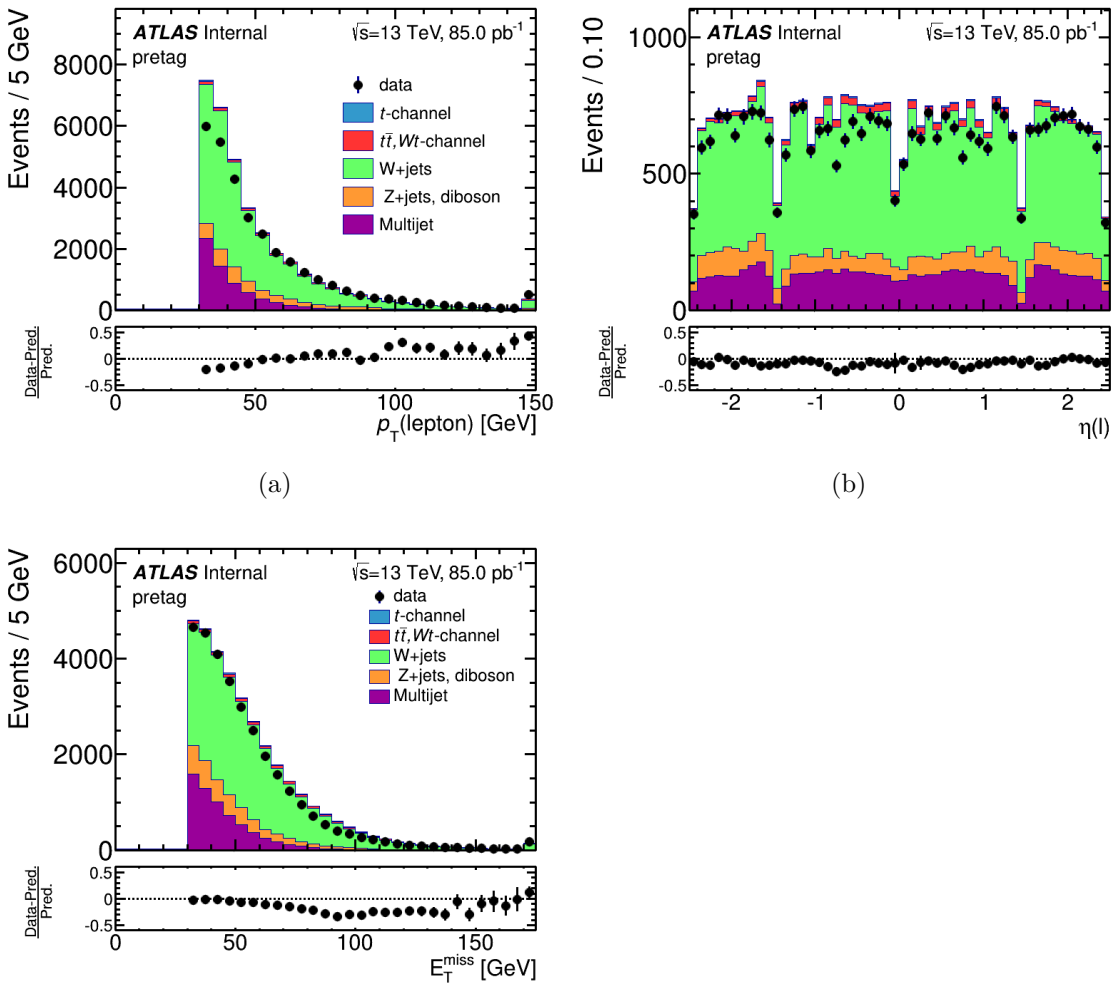

Figure 6.3: *Shown are the p_T (a) and pseudo rapidity (b) distributions of the lepton and the distribution of the missing transverse momentum (c). All distributions are normalized to the binned maximum-likelihood fit in the $m_T(W)$ distribution. In the lower panels the relative difference between MC events and observed data is shown for each bin.*

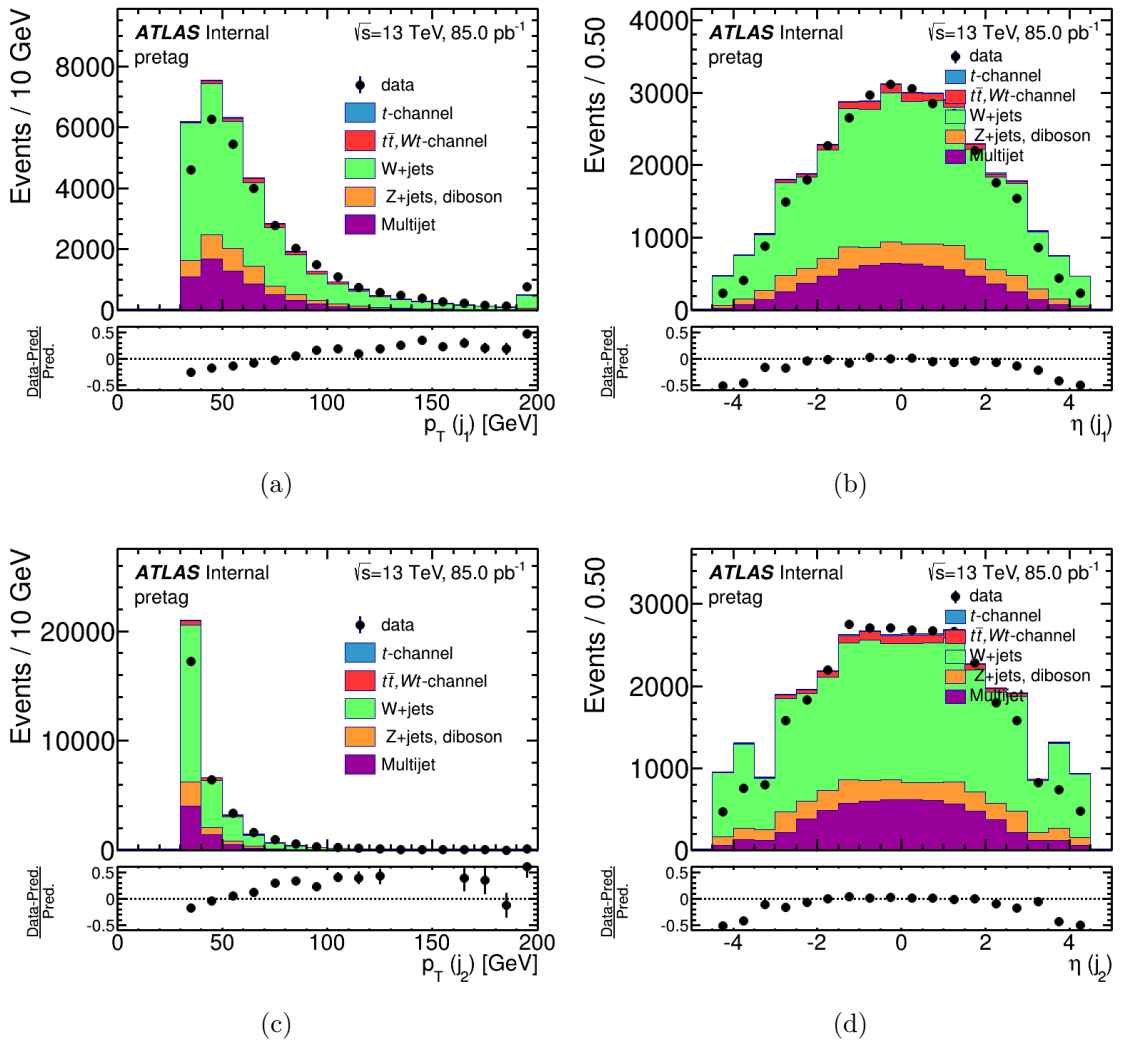

Figure 6.4: *Shown are the p_T and pseudo rapidity distributions of the leading jet (a),(b) and the second leading jet (c) and (d). All distributions are normalized to the binned maximum-likelihood fit in the $m_T(W)$ distribution. In the lower panels the relative difference between MC events and observed data is shown for each bin.*

7 Signal extraction

In the examined lepton+jets channel there is a large contribution of background events for the t-channel single top-quark process. No single variable can be used to efficiently separate signal and background events. Therefore in this thesis many kinematic variables are combined to one discriminant. Also the correlations of the variables are taken into account. This is done by using neural networks. This chapter contains a description of the applied neural network and the used input variables.

7.1 Neural networks

This analysis uses neural networks (NN) which are provided by the NeuroBayes package [42], [43]. The aim of a neural network is to calculate one output variable $NNout$ using several input variables. In a first step the input variables are preprocessed to get a better starting point for the training. The variables are decorrelated and for each variable the correlation to target is calculated. In an iterative procedure, the correlation loss of removing a given variable is calculated and the variables are ranked according to their significance.

This analysis uses a three-layer feed-forward NN. A schema of such a neural network is shown in figure 7.1. The layers are called input, hidden and output layer and consist of different numbers of nodes. In the input layer each variable is connected to one node. Additionally, one bias node is used. Each node of the input layer is connected with each hidden node. For each connection a weight is set in the training of the NN. Also all of the hidden nodes are adjunct with another weight to the output node.

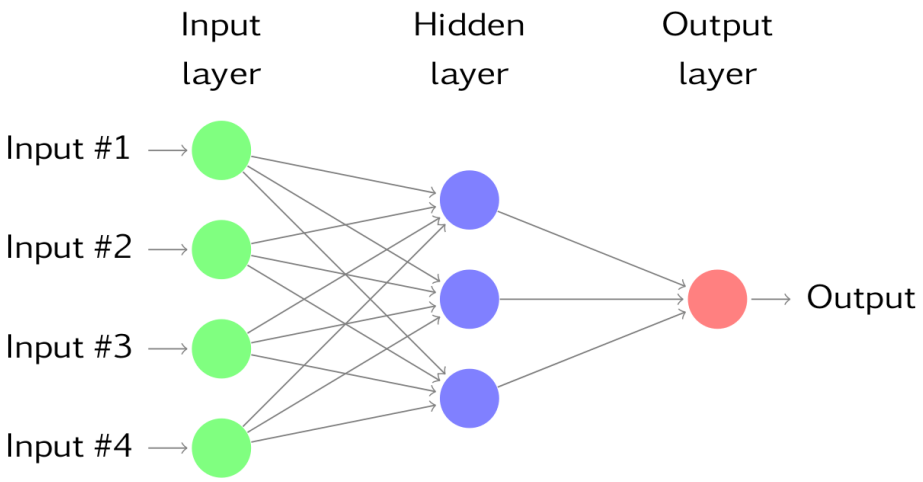

Figure 7.1: *Schema of a three-layer neural network with one output discriminant. The graphic is taken from Ref. [44]*

To use such a neural network as discriminant, the weights between the nodes have to be determined. Therefore MC simulations of signal and background processes are used to train the network. In a first step 80% of each sample is used with target values 1 for signal and 0 for background processes. Then the weights are fitted to receive the best target values. In this procedure low statistics or specific properties of input nodes can cause extreme output values. Therefore information is lost in the training, to avoid this so called over training. To additionally verify that there is no over training, the unused 20% of the samples are processed. Over training would cause extreme values in this verification. There was no over training seen in this analysis.

7.2 Input variables

To get an NN with a good discrimination between the t-channel single top-quark signal events and background events, it has to be trained with variables, which have different shapes for signal and background processes. Thus, not only the physics objects, like the lepton, missing transverse momentum, and jets are considered, but also reconstructed particles like the W-boson and the top-quark. One type of variables are basic kinematic variables like p_{T}, η, or the mass. But also H_{T}, differences in p_{T} of two particles or angular distances are studied. For the final NN only the 10 variables are used, that have the highest discrimination power.

In the following the most relevant input variables are described.

- $m(jb)$ is the mass of the four-vectors of the untagged jet and the b-tagged jet. The distributions for the SR and CR are shown in figure 7.2. The signal

process has a broader distribution than the background processes. This is because the t-channel top-quark production has a typical forward light jet, while the b-tagged jet is produced centrally. Therefore the invariant mass of those two is larger than in background events, where both jets are produced centrally.

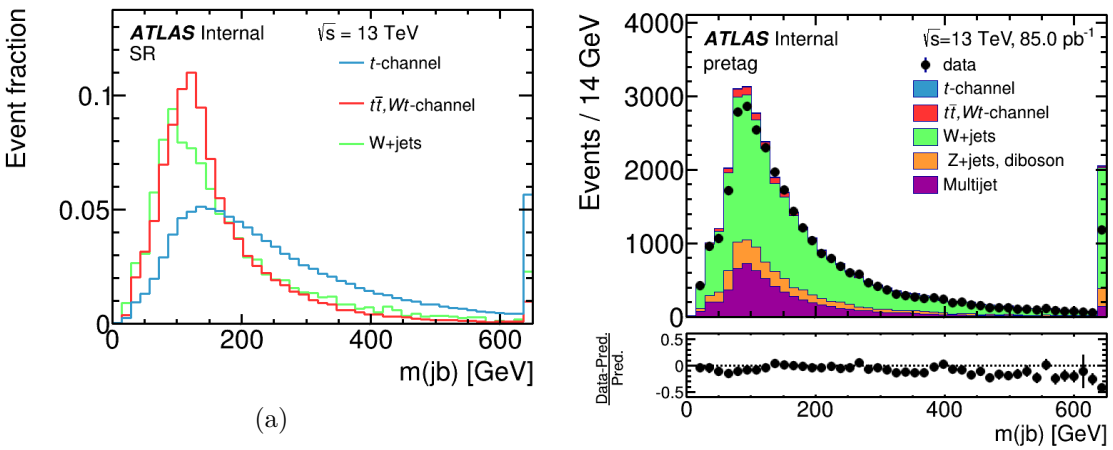

(a) (b)

Figure 7.2: *$m(jb)$ distribution for signal and the two dominant background processes normalized to unit area for the SR (a). Also for the CR (b) the $m(jb)$ distribution is shown, normalized to the binned maximum-likelihood fit of the $m_T(W)$ distribution. In the lower panel the relative difference between MC events and observed data is shown for each bin.*

- $m(l\nu b)$ is the mass of the charged lepton, the neutrino and the b-jet. Since these are the decay products of a top quark, this is the reconstructed top-quark mass in case of the signal process. Several other backgrounds contain real top quarks, however due to ambiguities in the jet assignment the reconstructed top-quark mass is much broader, as shown in Figure 7.3. In the W+jets process there is no top quark that could be reconstructed. Therefore the lower bound of the distribution is due to the applied cuts.

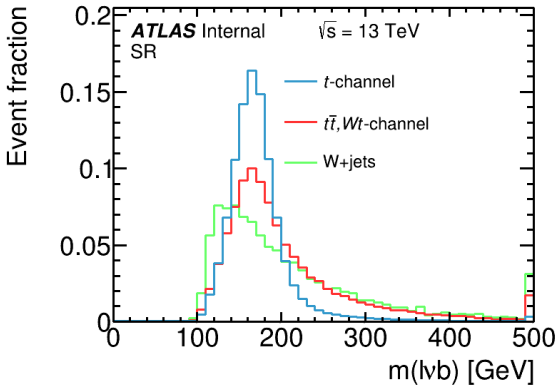

(a)

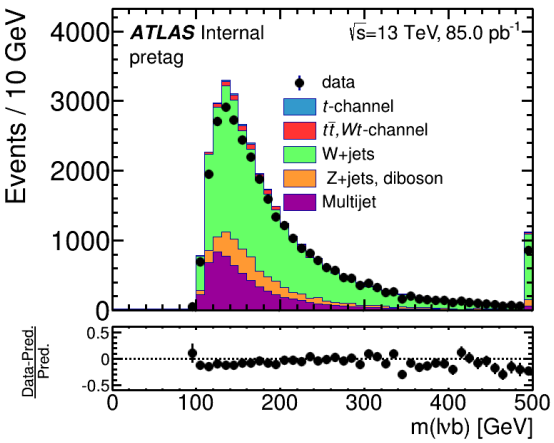

(b)

Figure 7.3: *$m(l\nu b)$ distribution for signal and the two dominant background processes normalized to unit area for the SR (a). Also for the CR (b) the $m(l\nu b)$ distribution is shown, normalized to the binned maximum-likelihood fit of the $m_T(W)$ distribution. In the lower panel the relative difference between MC events and observed data is shown for each bin.*

- $m_{\mathrm{T}}(W)$ is the transverse mass of the W-boson. The distributions for the SR and the CR are shown in Figure 7.4. The distribution for the $t\bar{t}$ process is broader than the one for t-channel single top-quarks, because they have two W-bosons in the final state.

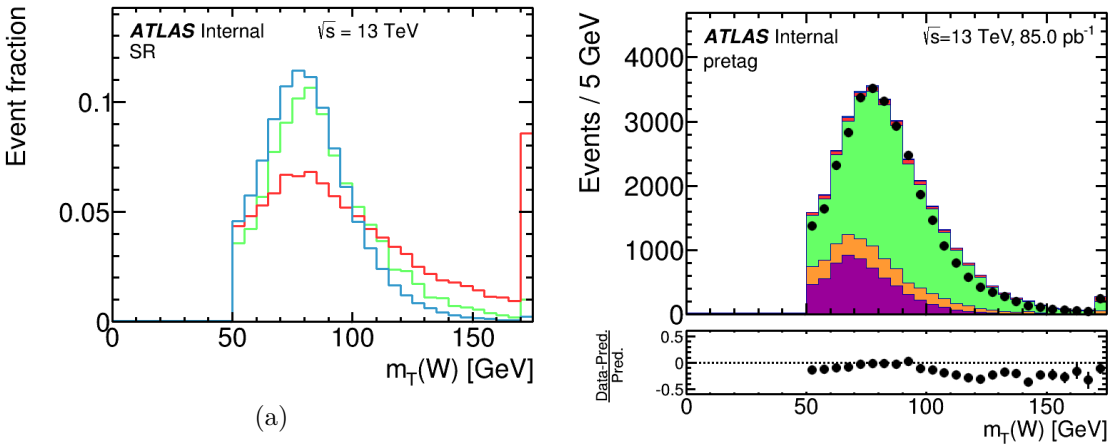

(a) (b)

Figure 7.4: *$m_T(W)$ distribution for signal and the two dominant background processes normalized to unit area for the SR (a). Also for the CR (b) the $m_T(W)$ distribution is shown, normalized to the binned maximum-likelihood fit of the $m_T(W)$ distribution. In the lower panel the relative difference between MC events and observed data is shown for each bin.*

- $\eta(j)$ is the pseudo rapidity of the light-quark jet. The distributions for the SR and the CR are shown in Figure 7.5. The light-quark jet in forward direction is one of the main characteristics of t-channel single top-quark production. Since light-quark jets are produced in decays in $t\bar{t}$ background events they are produced more isotropic. Therefore the forward jet has a good separation power to background events.

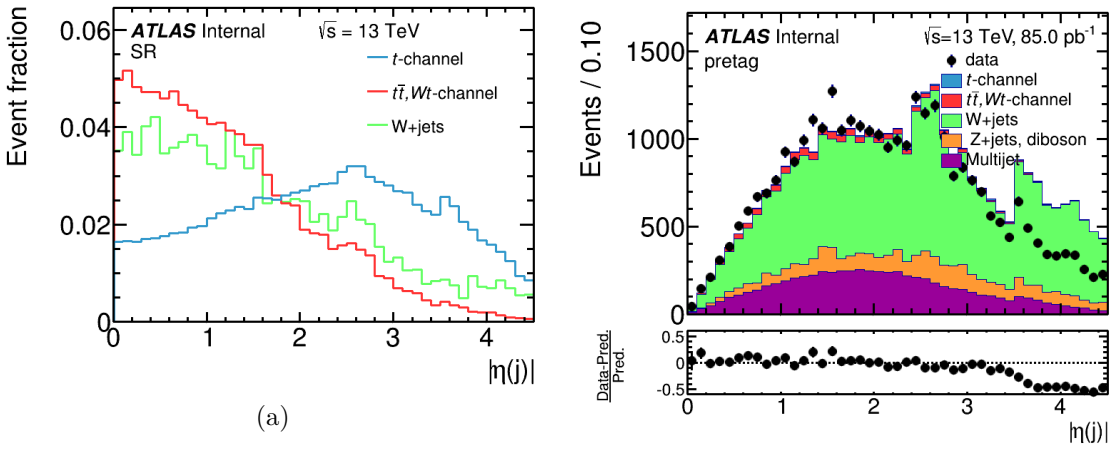

(a) (b)

Figure 7.5: $|\eta(j)|$ *distribution for signal and the two dominant background processes normalized to unit area for the SR (a). Also for the CR (b) the* $|\eta(j)|$ *distribution is shown, normalized to the binned maximum-likelihood fit of the* $m_T(W)$ *distribution. In the lower panel the relative difference between MC events and observed data is shown for each bin.*

7.3 Training results

In this analysis only one NN is trained. The training is done in the SR and the result is applied also in the CR. For the training the t-channel single top-quark process is set as signal, while the $t\bar{t}$, Wt, W+jets, Z+jet and diboson processes are background processes. The multijet background is not used in the training. A three-layer feed-forward neural network is used, with 10 input variables, 15 hidden nodes and one output node. The variables used in this analysis are listed in Table 7.1 together with their correlation loss. Additionally, to the variables described in the previous chapter, 6 other variables are used. $\Delta p_{\mathrm{T}}(j,t)$ is the difference in p_{T} of the light-quark jet and the reconstructed top-quark. $m(lb)$ is the mass of the combined lepton and b-tagged jet system. $\Delta R(t,j)$ is the distance of the reconstructed top-quark and the light jet in the (η,Φ) space. The polarization is the cosine of the pseudo rapidity between the light jet and the lepton in the rest frame of the reconstructed top-quark. $\eta(W)$ is the pseudo rapidity of the reconstructed W-boson. $dR(l,j)$ is the distance of the lepton and the light-quark jet in the (η,Φ) space.

For the SR the *NNout* distributions normalized to unit area are shown in Figure 7.6 for barrel electrons, end-cap electrons and muons separately and the combined distribution. Displayed are only the signal t-channel process with the two dominant

Table 7.1: *Variables used in the neural network with their correlation loss.*

rank	variables	corr. loss
1	$m(jb)$	17.58
2	$m(l\nu b)$	12.59
3	$m_{\mathrm{T}}(W)$	10.36
4	$\lvert\eta(j)\rvert$	12.72
5	$\Delta p_{\mathrm{T}}(j,t)$	8.72
6	$m(lb)$	8.75
7	$\Delta R(t,j)$	7.87
8	$\cos\Theta(l,j)_{l\nu b\mathrm{r.f.}}$	3.42
9	$\eta(W)$	8.16
10	$\Delta R(l,j)$	5.46

background processes, $t\bar{t}$ with Wt and W+jets. In all channels a good discrimination between signal and background is achieved.

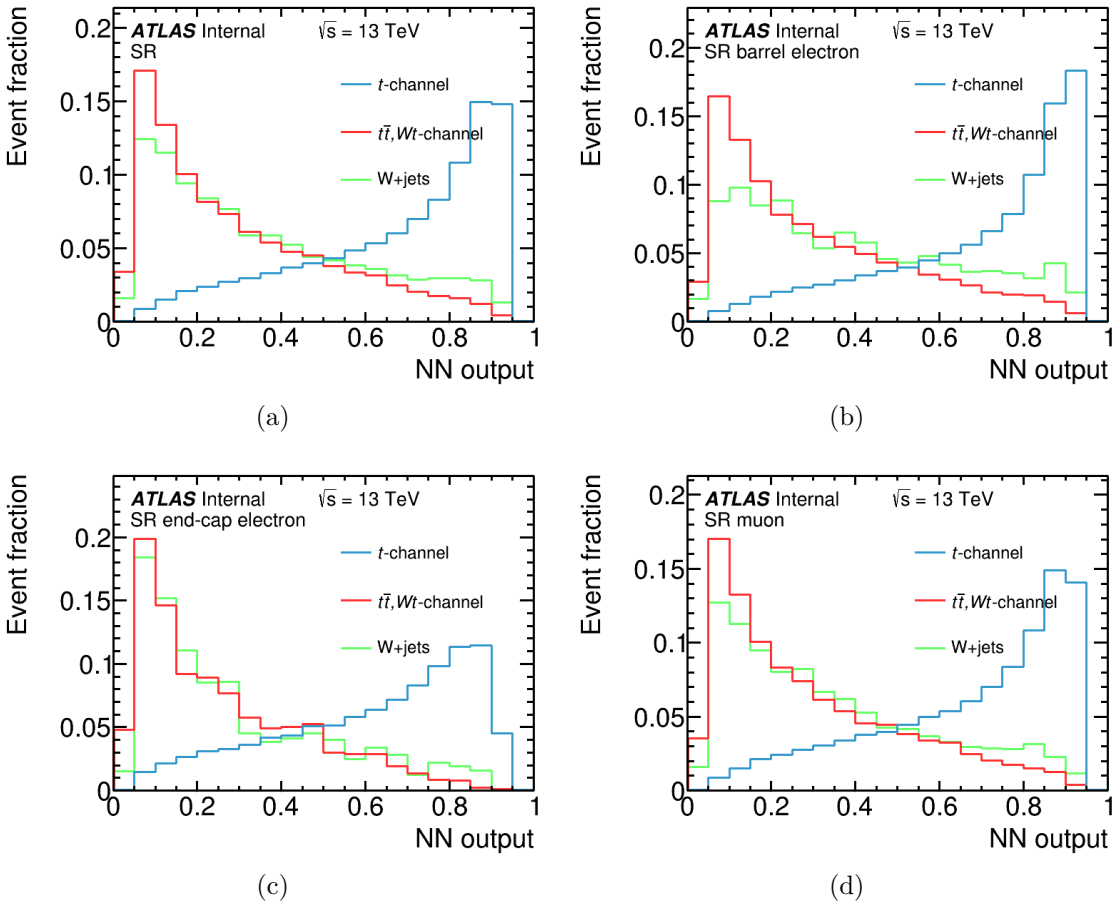

Figure 7.6: *Shown are the $NNout$ distributions for the SR normalized to unit area for the combined channel (a), the barrel (b) and end-cap (c) electrons and the muon channel (d).*

To study the modeling of the W+jets background the neural network, trained in the SR, is also applied to the CR. The $NNout$ distributions are shown in Figure 7.7 normalized to the observed data. Basically all expected distributions agree well with the observed data. Only for the barrel-electron distribution there are some events more expected in the high $NNout$ region.

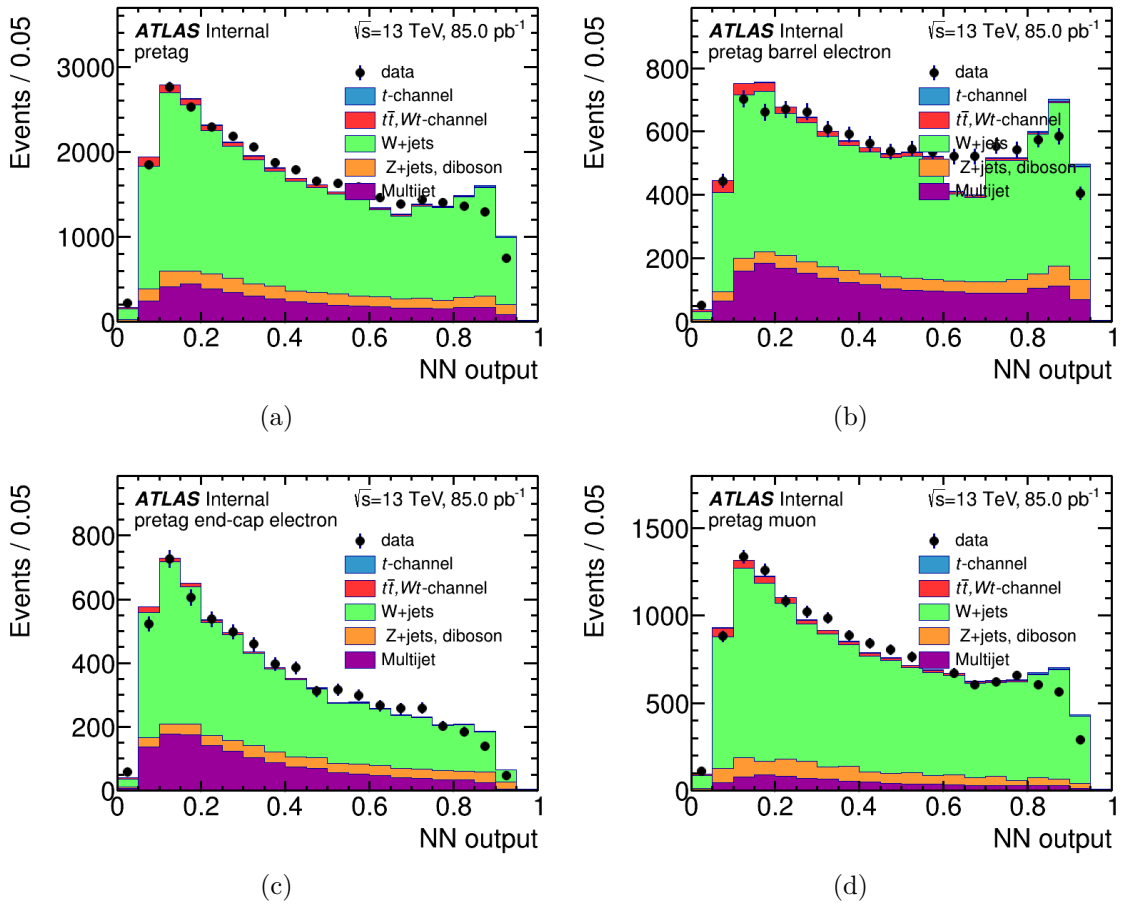

Figure 7.7: *Shown are the NNout distributions for the CR normalized to the observed data for the combined channel (a), the barrel (b) and end-cap (c) electrons and the muon channel (d).*

8 Cross-section measurement

The aim of this analysis is the measurement of the t-channel single top-quark cross section. Since the cross section is proportional to the number of expected events, the number of background events has to be estimated, to get the number of observed signal events. To get these numbers, a simultaneous binned maximum-likelihood fit is done for signal and background processes. The fit results are provided in the first part of this chapter, and the cross section is calculated in the second part.

8.1 Fit to the *NNout* discriminant

To get the number of signal and background events, a binned maximum-likelihood fit is done. In the fit a binned likelihood function L is maximized. The likelihood function is the product of Poisson functions P, which provide the content of each bin of the fitted distribution, and Gaussian functions G, which provide information of the background processes and the uncertainties.

$$L(\beta^s, \beta_j^b) = \prod_k P(n_k; \mu_k(\beta^s, \beta_j^b)) \times \prod_j G(\beta_j^b; 1, \Delta_j) \tag{8.1}$$

Here β^s is the scale factor for the measurement of $\sigma(tq + \bar{t}q)$ and β_j^b the scale factor the background process j. The index k is the number of the bin of the fitted distribution. n_k is the number of measured events in bin k and μ_k is the estimated number of signal and background events in bin k. Δ_j is the relative uncertainty on the number of predicted events of background process j.

A good distinction between background and signal processes is achieved in the neural network output discriminant. Therefore the fit is done in the $NNout$ variable. Since the Z+jets and diboson background has only a small contribution to the expected number of events, their number is fixed in the fit. Also the number of estimated multijet events, already estimated from data as discussed in chapter 6.1, is fixed in this fit. The $t\bar{t}$ and Wt processes are combined in this fit and the constraint for this process is set to the uncertainty of the theoretical prediction of 10%. Also the constrain for the W+jets process is set to the uncertainty of the theoretical prediction of 20%. The signal t-channel single top-quark process can vary freely in

the fit. The fit is done in the combined electron and muon channel, since the same cross section times branching ratio is expected and this method uses the highest statistics.

An event yield is given in Table 8.1. The number of Z+jets and diboson events is normalized to the theoretical prediction. The number of multijet events is estimated from data as discussed in chapter 6.1. The number of W+jets, $t\bar{t}$, Wt and t-channel events is estimated by the binned maximum-likelihood fit to the $NNout$ discriminant.

Table 8.1: *Estimated number of events for the different processes. Also the event fraction is provided.*

process	number of expected events	event fraction
t-channel	245	14.7 %
$t\bar{t}$,Wt-channel	762	45.7 %
W+jets	263	15.8 %
Z+jets,diboson	99	5.9 %
multijet	300	18.0 %

To validate the quality of the fit the expected distributions of the different processes are normalized to the fit result and the stacked histogram is compared to data. In Figure 8.1 the $NNout$ distribution is shown. The figure shows, that the expected distribution agrees well with the observed one. Especially for high $NNout$ values the contribution of the signal is visible. Also for the NN input variables the distributions after the fit are shown in Figures 8.2-8.3. There are some deviations of the MC samples and the observed data, especially in regions with low statistics. But there are also disagreements in regions with higher statistics, for example in the $\Delta p_{\mathrm{T}}(j, l\nu b)$ distribution. For low differences in the transverse momentum there are less events expected tan observed. The reason for this deviation can be the multijet background, which was produced with 8 TeV samples and applied to 13 TeV data.

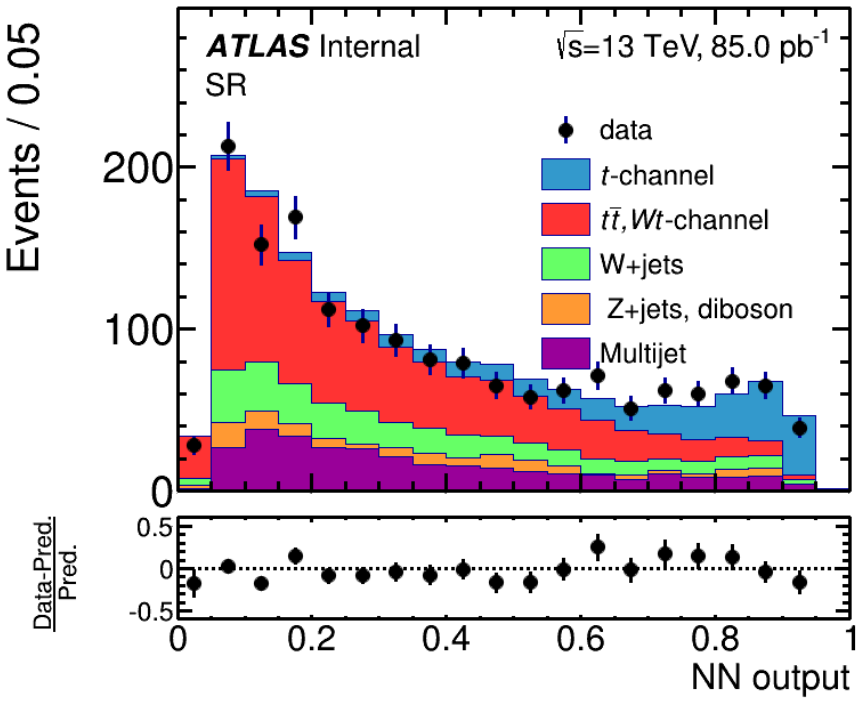

Figure 8.1: *Distribution of the NNout discriminant in the SR after the fit. In the lower panel the relative difference between MC events and observed data is shown for each bin.*

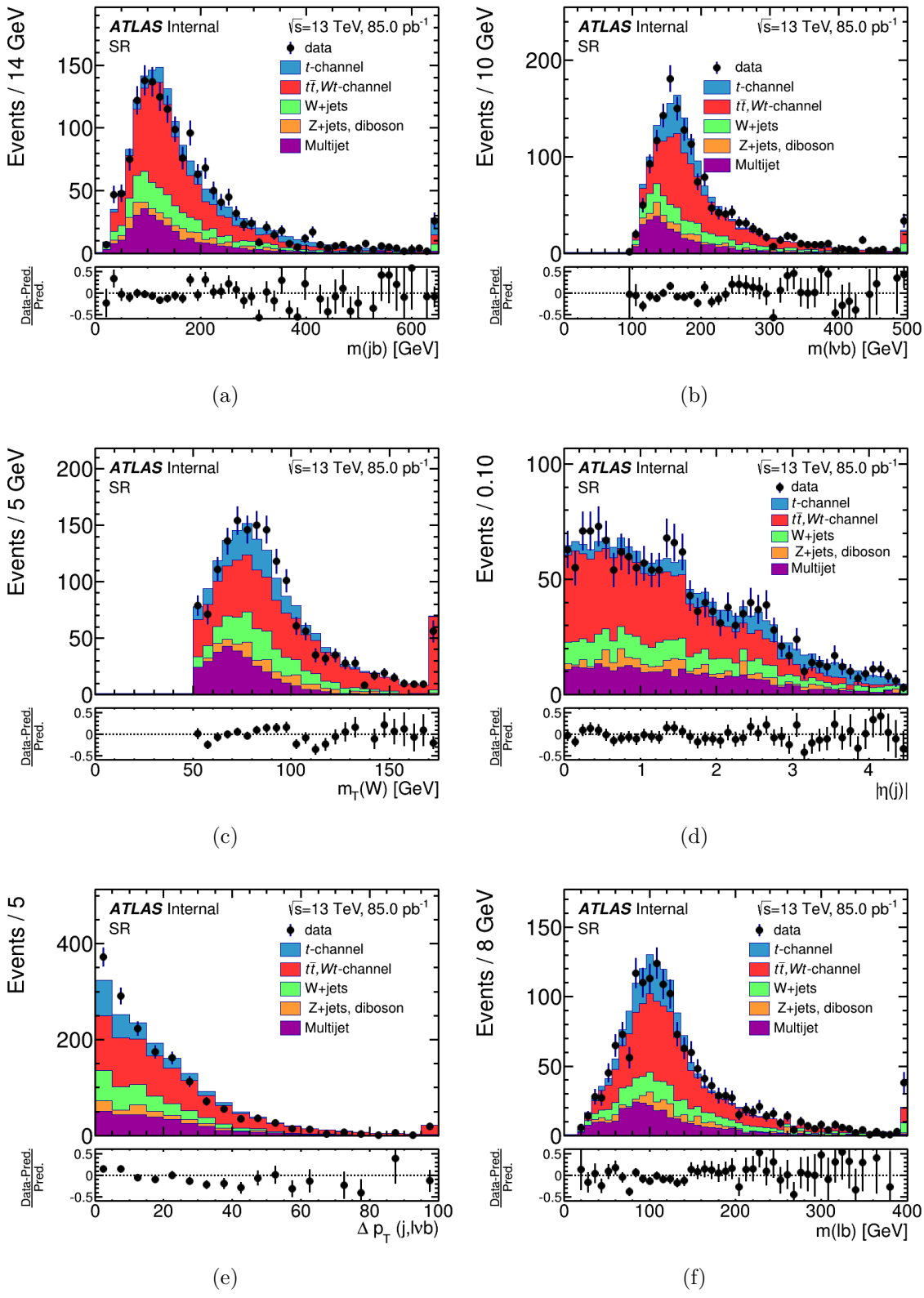

Figure 8.2: *Distributions of $m(jb)$ (a), $m(l\nu b)$ (b), $m_T(W)$ (c), $\eta(j)$ (d), $\Delta p_T(j,t)$ (e) and $m(lb)$ (f) in the SR after the fit. In the lower panels the relative difference between MC events and observed data is shown for each bin.*

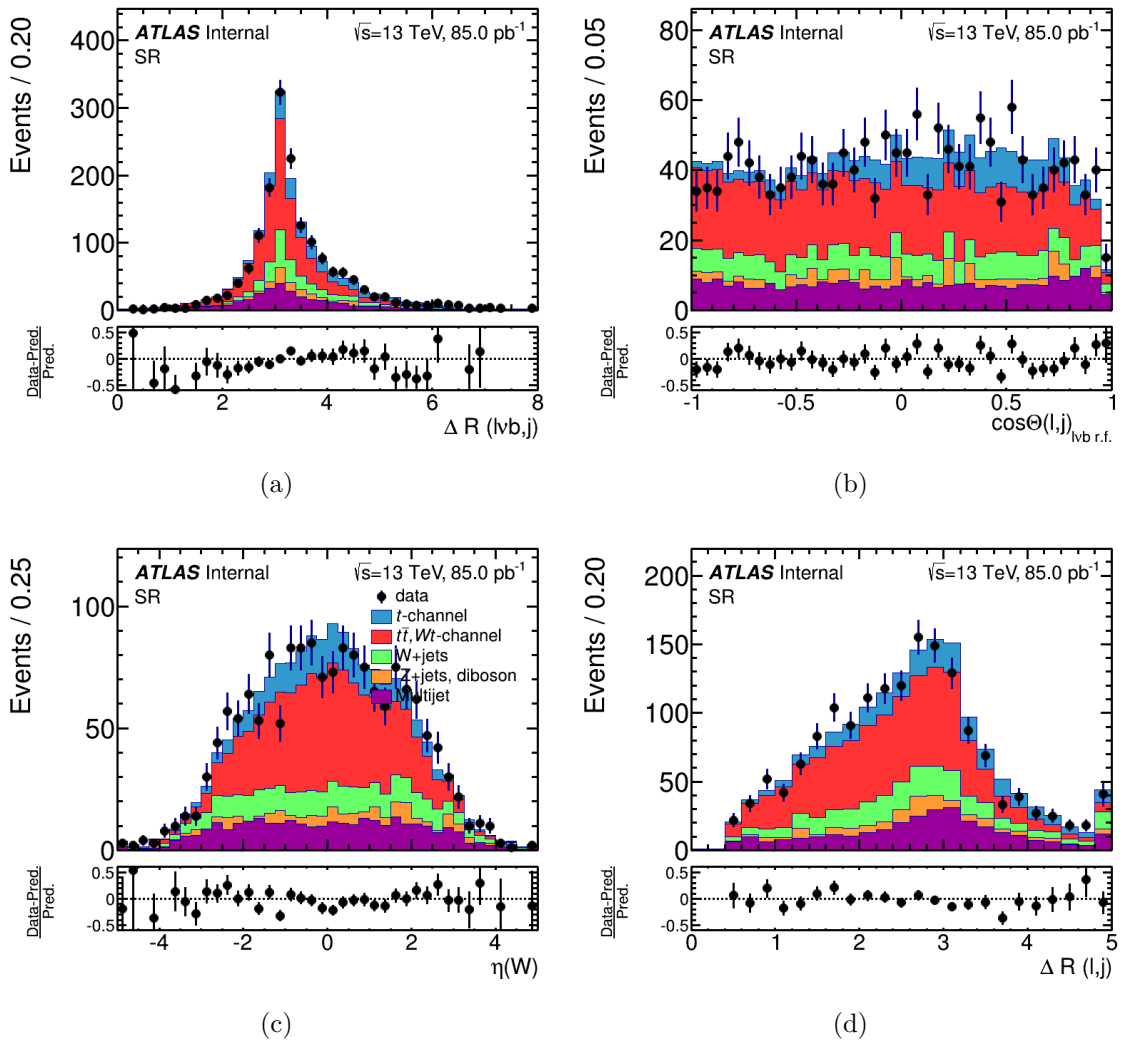

Figure 8.3: *Distributions of $\Delta R(t,j)$ (a), the angle between the charged lepton and the light-quark jet (b), $\eta(W)$ (c), and $dR(l,j)$ (d) in the SR after the fit. In the lower panels the relative difference between MC events and observed data is shown for each bin.*

8.2 Inclusive cross-section measurement

The result of the fit in the *NNout* distribution is a scale factor for the signal of $\beta^s = 1.12 \pm 0.14$. The scale factor is used to determine the t-channel single top-quark cross section to be :

$$\sigma(tq + \bar{t}q) = 240 \pm 30(\text{stat.}) \text{ pb}$$

The uncertainty of the result is statistical only and corresponds to a relative uncertainty of 12.5%. The theoretical prediction for the inclusive cross section is $\sigma^{theo.}_{tq+\bar{t}q} = 217.0^{+9.0}_{-7.7}$ pb and agrees with the measured value within its uncertainty.

9 Conclusion

In this analysis the cross section of the t-channel single top-quark production at $\sqrt{s} = 13$ TeV in proton-proton collisions was measured. The used dataset was taken with the ATLAS detector from June to July in 2015 and corresponds to an integrated luminosity of 85.0 pb^{-1}.

The lepton+jets channel is studied, where one charged lepton (electron or muon), a large amount of missing transverse momentum and exactly two jets, of which exactly one of them is b-tagged, are required. A few cuts are implemented to reduce as much background as possible, while the amount of signal events is only reduced a little. For further discrimination between signal and background a neural network is applied. The dominating backgrounds are the $t\bar{t}$ and the W+jets processes.

The inclusive t-channel cross section was measured to be $\sigma(tq + \bar{t}q) = 240.0 \pm 30(\text{stat.})$ pb with an assumed top-quark mass of $m_t = 172.5$ GeV. The measured value agrees well with the theoretical prediction of $\sigma^{theo.}_{tq+\bar{t}q} = 217.0^{+9.0}_{-7.7}$ pb.

This analysis can be improved, by using a larger dataset, to reduce the statistical uncertainty. Already at the end of August 2015 about two times more data has been taken with the ATLAS detector and there are more runs planned in 2015 at $\sqrt{s} = 13$ TeV. Also software infrastructure to estimate some of the systematic uncertainties is now available.

List of Figures

2.1 Elementary particles of the standard model. The graphic is taken from Ref. [8]. 3
2.2 Feynman diagrams for the $t\bar{t}$ production with gluons. The graphic is taken from Ref. [12]. 5
2.3 Parton distribution functions of the proton at the energy scale $Q^2 = 10\ GeV^2$ and $Q^2 = 10^4\ GeV^2$. The graphic is taken from Ref. [15]. . . 6
2.4 Feynman diagrams of single-top (a) t-channel, (b) associated Wt, and (c) s-channel production. The graphic is taken from Ref. [16] 6
2.5 Feynman diagrams of the top-quark background processes. The $t\bar{t}$ process with semi-leptonic decay (a), the associated Wt production (b), and the single top-quark s-channel production (c). The graphic is taken from Ref. [17] 7
2.6 Cross sections of different processes for different center of mass energies. The graphic is taken from Ref. [18] 8
2.7 Feynman diagrams of the W+jets (a) and the multijet (b) background. The graphic is taken from Ref. [17] 9
2.8 Feynman diagrams of the Z+jets (a) and the diboson backgrounds. For the diboson processes, a WW (b), a WZ (c) and a ZZ (d) diagram is shown. The graphic is taken from Ref. [17] 9

3.1 Schema of the different accelerators at CERN. The graphic is taken from Ref. [20]. 12
3.2 Schema of the ATLAS detector. The graphic is taken from Ref. [22]. 14
3.3 Integrated luminosity delivered by LHC and recorded by ATLAS from June till August 2015. The graphic is taken from Ref. [23]. 16

4.1 Schema of a proton-proton collision. Shown are the different types of interactions occurring in a single proton-proton collision. The graphic is taken from Ref. [24]. 20

6.1 Shown are the $m_{\mathrm{T}}(W)$ distributions after the QCD fit for all channels in the SR. In the lower panels the relative difference between MC events and observed data is shown for each bin. 31

6.2 Shown are the $m_{\mathrm{T}}(W)$ distributions after the binned maximum-likelihood fit in the $m_{\mathrm{T}}(W)$ distribution for all channels in the CR. In the lower panels the relative difference between MC events and observed data is shown for each bin. 32
6.3 Shown are the p_{T} (a) and pseudo rapidity (b) distributions of the lepton and the distribution of the missing transverse momentum (c). All distributions are normalized to the binned maximum-likelihood fit in the $m_{\mathrm{T}}(W)$ distribution. In the lower panels the relative difference between MC events and observed data is shown for each bin. 34
6.4 Shown are the p_{T} and pseudo rapidity distributions of the leading jet (a),(b) and the second leading jet (c) and (d). All distributions are normalized to the binned maximum-likelihood fit in the $m_{\mathrm{T}}(W)$ distribution. In the lower panels the relative difference between MC events and observed data is shown for each bin. 35

7.1 Schema of a three-layer neural network with one output discriminant. The graphic is taken from Ref. [44] 38
7.2 $m(jb)$ distribution for signal and the two dominant background processes normalized to unit area for the SR (a). Also for the CR (b) the $m(jb)$ distribution is shown, normalized to the binned maximum-likelihood fit of the $m_{\mathrm{T}}(W)$ distribution. In the lower panel the relative difference between MC events and observed data is shown for each bin. 39
7.3 $m(l\nu b)$ distribution for signal and the two dominant background processes normalized to unit area for the SR (a). Also for the CR (b) the $m(l\nu b)$ distribution is shown, normalized to the binned maximum-likelihood fit of the $m_{\mathrm{T}}(W)$ distribution. In the lower panel the relative difference between MC events and observed data is shown for each bin. 40
7.4 $m_{\mathrm{T}}(W)$ distribution for signal and the two dominant background processes normalized to unit area for the SR (a). Also for the CR (b) the $m_{\mathrm{T}}(W)$ distribution is shown, normalized to the binned maximum-likelihood fit of the $m_{\mathrm{T}}(W)$ distribution. In the lower panel the relative difference between MC events and observed data is shown for each bin. 41
7.5 $|\eta(j)|$ distribution for signal and the two dominant background processes normalized to unit area for the SR (a). Also for the CR (b) the $|\eta(j)|$ distribution is shown, normalized to the binned maximum-likelihood fit of the $m_{\mathrm{T}}(W)$ distribution. In the lower panel the relative difference between MC events and observed data is shown for each bin. 42

7.6 Shown are the *NNout* distributions for the SR normalized to unit area for the combined channel (a), the barrel (b) and end-cap (c) electrons and the muon channel (d). 44
7.7 Shown are the *NNout* distributions for the CR normalized to the observed data for the combined channel (a), the barrel (b) and end-cap (c) electrons and the muon channel (d). 45

8.1 Distribution of the *NNout* discriminant in the SR after the fit. In the lower panel the relative difference between MC events and observed data is shown for each bin. 49
8.2 Distributions of $m(jb)$ (a), $m(l\nu b)$ (b), $m_{\mathrm{T}}(W)$ (c), $\eta(j)$ (d), $\Delta p_{\mathrm{T}}(j,t)$ (e) and $m(lb)$ (f) in the SR after the fit. In the lower panels the relative difference between MC events and observed data is shown for each bin. 50
8.3 Distributions of $\Delta R(t,j)$ (a), the angle between the charged lepton and the light-quark jet (b), $\eta(W)$ (c), and $dR(l,j)$ (d) in the SR after the fit. In the lower panels the relative difference between MC events and observed data is shown for each bin. 51

List of Tables

3.1 List of runs used in this analysis. Also the peak and integrated luminosity for each run is listed [23]. 17

4.1 List of used samples generated with Powheg and Pythia. Also $\sigma \times \mathcal{B}$ is listed. 22
4.2 List of used diboson samples generated with Sherpa. Also $\sigma \times \mathcal{B}$ is listed. 22
4.3 List of used W+jets samples generated with Sherpa. Also $\sigma \times \mathcal{B}$ is listed. 23
4.4 List of used Z+jets samples generated with Sherpa. Also $\sigma \times \mathcal{B}$ is listed. 24

6.1 Estimated event fraction of multijet events after applying additionally the $m_{\mathrm{T}}(W)$ cut. 30

7.1 Variables used in the neural network with their correlation loss. . . . 43

8.1 Estimated number of events for the different processes. Also the event fraction is provided. 48

Bibliography

[1] ATLAS Collaboration, CDF Collaboration, CMS Collaboration, and DØ Collaboration, First combination of Tevatron and LHC measurements of the topquark mass, Tech. rep. ATLAS-CONF-2014-008. CDF-NOTE-11071. CMSPAS-TOP-13-014. D0-NOTE-6416. CERN, Fermilab, Mar. 2014. arXiv:1403.4427 [hep-ex].

[2] ATLAS Collaboration, Comprehensive measurements of t-channel single top-quark production cross sections at $\sqrt{s} = 7$ TeV with the ATLAS detector, Phys. Rev. D 90 (2014) 112006, arXiv: 1406.7844 [hep-ex].

[3] ATLAS Collaboration, Measurement of the t-channel single top-quark production cross section in pp collisions at $\sqrt{s} = 7$ TeV with the ATLAS detector, Phys. Lett. B 717 (2012) 330, arXiv: 1205.3130 [hep-ex].

[4] CMS Collaboration, Measurement of the t-channel single top quark production cross section in pp collisions at $\sqrt{s} = 7$ TeV, Phys. Rev. Lett. 107 (2011) 091802, arXiv: 1106.3052 [hep-ex].

[5] ATLAS Collaboration, Measurement of t-Channel Single Top-Quark Production in pp Collisions at $\sqrt{s} = 8$ TeV with the ATLAS detector, ATLAS-CONF-2012-132, 2012, url: http://cdsweb.cern.ch/record/1478371.

[6] CMS Collaboration, Measurement of the t-channel single-top-quark production cross section and of the V_{tb} CKM matrix element in pp collisions at $\sqrt{s} = 8$ TeV, JHEP 1406 (2014) 090, arXiv: 1403.7366 [hep-ex].

[7] N. Kidonakis, Next-to-next-to-leading-order collinear and soft gluon corrections for t-channel single top quark production, Phys. Rev. D 83 (2011) 091503, eprint: arXiv:1103.2792.

[8] https://upload.wikimedia.org/wikipedia/commons/0/00/ Standard_Model_of_Elementary_Particles.svg

[9] D. Griffiths. Introduction to Elementary Particles. Weinheim, Germany: WILEY-VCH, 2008. isbn: 3527406018.

[10] N. Cabibbo, Unitary Symmetry and Leptonic Decays, Phys. Rev. Lett. 10 (1963).

[11] M. Kobayashi and T. Maskawa, CP-Violation in the Renormalizable Theory of Weak Interaction, Prog. Theor. Phys. 49 (1973).

[12] http://inspirehep.net/record/780632/files/Pics_gg-ttbar.png

[13] Jun Gao, Pavel Nadolsky, A meta-analysis of parton distribution functions arXiv:1401.0013 [hep-ph]

[14] Hung-Liang Lai, Marco Guzzi, Joey Huston, Zhao Li, Pavel M. Nadolsky, Jon Pumplin, C.-P. Yuan, New parton distributions for collider physics, arXiv:1007.2241 [hep-ph]

[15] http://nnpdf.hepforge.org/

[16] http://cds.cern.ch/record/1668960/?ln=de figure1

[17] http://elpub.bib.uni-wuppertal.de/servlets/DerivateServlet/Derivate-4650/dc1436.pdf

[18] http://inspirehep.net/record/805147/files/crosssections2008.png

[19] The ATLAS Collaboration, Luminosity Determination in pp Collisions at sqrt(s)=7 TeV Using the ATLAS Detector at the LHC, arXiv:1101.2185 [hep-ex]

[20] http://www.boincitaly.org/forum/astronomia-fisica-e-chimica/171-thread-ufficiale-lhc-home.html

[21] ATLAS Collaboration, The ATLAS Experiment at the CERN Large Hadron Collider, JINST 3 (2008) S08003.

[22] http://inspirehep.net/record/878496/plots

[23] https://atlas.web.cern.ch/Atlas/GROUPS/DATAPREPARATION/DataSummary/

[24] http://www.isgtw.org/feature/sherpa-and-open-science-grid-predicting-emergence-jets

[25] S. Alioli et al., A general framework for implementing NLO calculations in shower Monte Carlo programs: the POWHEG BOX, JHEP 06 (2010) 043, arXiv: 1002.2581 [hep-ph].

[26] S. Alioli et al., NLO single-top production matched with shower in POWHEG: s- and t-channel contributions, JHEP 09 (2009) 111, [Erratum: JHEP02,011(2010)], arXiv: 0907.4076 [hep-ph].

[27] T. Sjostrand, S. Mrenna and P. Z. Skands, A Brief Introduction to PYTHIA 8.1, Comput. Phys. Commun. 178 (2008) 852, arXiv: 0710.3820.

[28] M. Bahr, S. Gieseke, M. A. Gigg, D. Grellscheid, K. Hamilton, O. Latunde-Dada, S. Platzer, P. Richardson, M. H. Seymour, A. Sherstnev, J. Tully, B. R. Webber, Herwig++ Physics and Manual, arXiv:0803.0883 [hep-ph]

[29] T. Gleisberg et al., Event generation with SHERPA 1.1, JHEP 0902 (2009) 007, arXiv: 0811.4622 [hep-ph].

[30] J. Alwall, R. Frederix, S. Frixione, V. Hirschi, F. Maltoni, O. Mattelaer, H.-S. Shao, T. Stelzer, P. Torrielli, M. Zaro, The automated computation of tree-level and next-to-leading order differential cross sections, and their matching to parton shower simulations, arXiv:1405.0301 [hep-ph]

[31] https://twiki.cern.ch/twiki/bin/viewauth/AtlasProtected/TopDerivationMC15List

[32] T. Cornelissen et al. Concepts, Design and Implementation of the ATLAS New Tracking (NEWT). Tech. rep. ATL-SOFT-PUB-2007-007. Geneva, Switzerland: CERN, Mar. 2007. url: http://cds.cern.ch/record/1020106.

[33] R. E. Kalman. A New Approach to Linear Filtering and Prediction Problems. J. Fluids Eng. 82.1 (1960), pp. 35-45.

[34] R. Fruhwirth. Application of Kalman filtering to track and vertex fitting. Nucl. Instrum. Meth. A262 (1987), pp. 444-450.

[35] G. Piacquadio, K. Prokofiev, and A. Wildauer. Primary vertex reconstruction in the ATLAS experiment at LHC. J. Phys. Conf. Ser. 119 (2008), p. 032033.

[36] ATLAS Collaboration. Electron performance measurements with the ATLAS detector using the 2010 LHC proton-proton collision data. Eur. Phys. J. C 72 (2012), p. 1909. arXiv:1110.3174 [hep-ex].

[37] ATLAS Collaboration. Muon reconstruction efficiency and momentum resolution of the ATLAS experiment in proton-proton collisions at $\sqrt{s} = 7$ TeV in 2010. Eur. Phys. J. C 74.9 (2014), p. 3034. arXiv:1404.4562 [hep-ex].

[38] W. Lampl et al. Calorimeter Clustering Algorithms: Description and Performance. Tech. rep. ATL-LARG-PUB-2008-002. Geneva, Switzerland: CERN, Apr. 2008. url: http://cds.cern.ch/record/1099735.

[39] ATLAS Collaboration. Performance of Missing Transverse Momentum Reconstruction in Proton-Proton Collisions at 7 TeV with ATLAS. Eur. Phys. J. C 72 (2012), p. 1844. arXiv:1108.5602 [hep-ex].

[40] P. Sturm and W. Wagner. Measurement of the t-Channel Single Top-Quark Production Cross-Section with the ATLAS Detector at $\sqrt{s} = 7$ TeV. Presented 01 June 2012. PhD thesis. Wuppertal, Germany: Wuppertal U., Nov. 2012. url: http://elpub.bib.uni-wuppertal.de/edocs/dokumente/fbc/physik/diss2012/sturm.

[41] M. Cacciari, G. P. Salam and G. Soyez, The Anti-k(t) jet clustering algorithm, JHEP 0804 (2008) 063, http://fastjet.fr/, arXiv: 0802.1189.

[42] Michael Feindt, A Neural Bayesian Estimator for Conditional Probability Densities, (2004), arXiv:physics/0402093 [physics.data-an]

[43] M. Feindt and U. Kerzel, The NeuroBayes Neural Network Package, Nucl. Instrum. Meth. A559 (2006) 190.

[44] https://www.otexts.org/fpp/9/3

Selbstständigkeitserklärung / Eidesstattliche Erklärung

Der Verfasser erklärt an Eides statt, dass er die vorliegende Arbeit selbständig, ohne fremde Hilfe und ohne Benutzung anderer als die angegebenen Hilfsmittel angefertigt hat. Die aus fremden Quellen (einschliesslich elektronischer Quellen) direkt oder indirekt übernommenen Gedanken sind ausnahmslos als solche kenntlich gemacht. Die Arbeit ist in gleicher oder ähnlicher Form oder auszugsweise im Rahmen einer anderen Prüfung noch nicht vorgelegt worden.

Wuppertal, October 13, 2015